

The optical photometric and spectroscopic periodicities of the cataclysmic variable SRGt 062340.2-265751

J. Brink ^{1,2,3,4}, D.A.H. Buckley^{3,4,5}, M. Veresvarska⁶, A.D. Schwope¹, P.J. Groot^{3,4,7}, J.R. Thorstensen⁸, V. A. Cúneo¹, S.B. Potter^{3,9}, N. Titus³, D. Egbo^{3,4}, R. Lees^{3,4}, O. Mogawana^{3,4}, and A. van Dyk^{3,4}

¹ Leibniz-Institut für Astrophysik Potsdam (AIP), An der Sternwarte 16, 14482 Potsdam, Germany

² Institute for Physics and Astronomy, University of Potsdam, Karl-Liebknecht-Str. 24/25, 14476 Potsdam, Germany

³ South African Astronomical Observatory, PO Box 9, Observatory Road, Observatory 7935, Cape Town, South Africa

⁴ Department of Astronomy, University of Cape Town, Private Bag X3, Rondebosch 7701, South Africa

⁵ Department of Physics, University of the Free State, PO Box 339, Bloemfontein 9300, South Africa

⁶ Department of Physics, Centre for Extragalactic Astronomy, Durham University, South Road, Durham DH1 3LE, UK

⁷ Department of Astrophysics/IMAPP, Radboud University, PO Box 9010, NL-6500GL Nijmegen, the Netherlands

⁸ Department of Physics and Astronomy, Dartmouth College, Hanover NH 03755, USA

⁹ Department of Physics, University of Johannesburg, PO Box 524, Auckland Park 2006, South Africa

Received 27 August 2025; accepted 13 January 2026

ABSTRACT

Context. We report on optical spectroscopic and photometric follow-up observations of the eROSITA discovered transient SRGt 062340.2-265751 and show that it displays the characteristics of a nova-like cataclysmic variable (CV), with possible indications of being a magnetic system.

Aims. We try to put better constraints on the classification of SRGt 062340.2-265751 using optical time-resolved spectroscopic and photometric observations to find any periodicities in the system. From these periodicities we can classify the CV sub-type that it belongs to.

Methods. Time-resolved photometric and spectroscopic observations were obtained at the South African Astronomical Observatory (SAAO), using the 1.9m and the two 1.0m telescopes. High-resolution spectra were also taken using the Southern African Large Telescope (SALT), to study the morphology of the emission lines seen in the system. Archival photometric data was also analysed in this study, including ASAS-SN, CRTS, and *TESS* observations.

Results. Spectroscopic observations revealed a very low amplitude, $K \sim 14 \text{ km s}^{-1}$, in the radial velocity of the $H\beta$ and $H\gamma$ emission lines, suggesting that the system is likely observed at a low inclination angle. High-speed photometric observations revealed highly stochastic variability, characteristic of many magnetic cataclysmic variable systems. A probable 3.645 ± 0.006 hour orbital period was found by applying Lomb-Scargle period analysis to the $H\beta$ and $H\gamma$ emission line radial velocities. A 24.905 ± 0.065 min period was found from photometric observations, which we associate with the white dwarf spin. However, it was also found that the photometry revealed multiple periodicities from night to night. *TESS* observations in three sectors did not reveal any of the periodicities found from ground-based observations, but did show a prominent period in only one sector, which might be attributed to a positive superhump period. These multiple periodicities as well as the $\text{He II } \lambda 4686$ and Bowen blend emission lines seen in the spectra indicate that SRGt 062340.2-265751 is likely a nova-like CV, and might belong to the VY Scl sub-type.

Key words. binaries: close – novae, cataclysmic variables – X-rays: binaries

1. Introduction

Cataclysmic variables (CVs) are binary systems, with orbital periods typically of a few hours, consisting of a white dwarf (WD) primary together with a Roche lobe filling secondary star (also called the donor or companion) that is generally of a low-mass main-sequence spectral class (for a detailed description of CVs see [Warner 1995](#)). As the companion overflows its Roche lobe, material flows towards the WD through the inner Lagrangian point, $L1$. The magnetic field of the WD, however, strongly dictates how the material flows as it leaves $L1$. In systems with a weakly magnetized WD ($B \lesssim 10^5 \text{ G}$), an accretion disc forms that may extend all the way to the surface of the WD. In contrast, in AM Her systems, or polars, the WD is strongly magnetized ($B > 10^7 \text{ G}$), the WD spin and binary periods are synchronized, and no accretion disc forms. Material is directly channelled by

the magnetic field lines of the WD at $L1$ ([Schwope 2025](#)). This causes the material to leave the orbital plane and flow directly to the WD's magnetic poles. Due to the strong magnetic field, polars have synchronized (or very nearly) WD spin and binary orbital periods.

In CVs that contain a WD with a weaker magnetic field, known as intermediate polars (IPs) or DQ Her systems, an accretion disc may form that gets truncated at the magnetospheric radius of the WD. Material from the disc flows towards the WD in accretion curtains that rise above and/or below the orbital plane. This, together with the asynchronous WD spin and binary orbital periods, creates a rich phenomenology in periodicities in IPs.

Disc accreting CVs are further subdivided into the low-accretion-rate dwarf novae (DNe) and the high-mass-transfer-rate nova-likes (NLs). The CVs can be further subdivided based on their spectroscopic and/or photometric properties. One of these subclasses is the VY Sculptoris (VY Scl) system, which

* jbrink@aip.de

has a distinct characteristic of going into low states at random without showing any outburst (Hellier 2001). These low states are easily identified in optical light curves. It was also suggested by Hameury & Lasota (2002) that VY Scl systems should host a magnetic WD, with similar magnetic field strengths to that found in IPs, to prevent DN outbursts during low states.

SRGt 062340.2-265751, hereafter SRGt 062340, was first reported by Denis Denisenko as a possible NL and VY Scl type variable in April 2017, and given the designation DDE 79¹. It was later detected as a transient X-ray source (Schwope et al. 2022) by both instruments, the Mikhail Pavlinsky Astronomical Roentgen Telescope - X-ray Concentrator (ART-XC, Pavlinsky et al. 2021), and the extended ROentgen Survey with an Imaging Telescope Array (eROSITA, Predehl et al. 2021), during the second all-sky survey of the Spektrum-Roentgen-Gamma (SRG, Sunyaev et al. 2021) mission. It was also previously detected and catalogued as a transient by The Zwicky Transient Facility (ZTF19aaabzuh), Swift/XRT (2SXPS J062339.9-265751) and ROSAT (1RXS J062339.8-265744), where it was cross-matched² to a USNO A2 optical counterpart of $B=12.7$ mag with a fractional probability of 0.952. Gaia DR3 (Gaia DR3 2899766827964264192) measured a parallax of $\pi = 1.9749 \pm 0.0192$ mas, giving a geometric distance of 495.5 ± 4.0 pc (following Bailer-Jones et al. 2021), and mean $G = 12.436 \pm 0.005$ mag, giving it an absolute G-band magnitude of $M_G = 3.96$ mag, absorption not considered. Initial spectroscopic follow-up observations were made using the Wide Field Spectrograph (WiFeS, Dopita et al. 2010) on the Australian National University's 2.3 m telescope, covering $\lambda 3500 - 5500 \text{ \AA}$, and the High-Resolution Spectrograph (HRS, Barnes et al. 2008; Crause et al. 2014) on the 10m-class Southern African Large Telescope (SALT, Buckley et al. 2006), covering $\lambda 3800 - 8900 \text{ \AA}$ (Schwope et al. 2022).

These spectroscopic observations revealed a continuum that is very blue. The HRS spectrum clearly shows the He II $\lambda 4686$ emission line as well as the C III/N III Bowen blend (C III components at 4647.4 \AA and 4650.1 \AA , as well as N III components at 4634.13 \AA and 4640.64 \AA), a feature that is encountered in the spectra of magnetic CVs, i.e. polars and IPs, (Schachter et al. 1991; Harlaftis & Horne 1999), and also in some nova-like CVs and low-mass X-ray binaries (LMXBs), which indicates strong UV/EUV/X-ray emission. The WiFeS observations revealed broad Balmer absorption lines with centres filled with prominent emission lines, as well as neutral and ionized helium emission lines. The full widths at half maximum (FWHMs) of the Balmer emission lines were observed to be $300-380 \text{ km s}^{-1}$, while those of the absorption lines corresponding to 3000 km s^{-1} . The FWHM of the He II $\lambda 4686$ line was $\sim 380 \text{ km s}^{-1}$, although the line was fairly weak. A 65 km s^{-1} difference in velocity was measured between the WiFeS and HRS observations, which illustrated that a follow-up orbital radial velocity study of the object was viable.

Schwope et al. (2022) also reported on two observations of SRGt 062340 obtained with the Transiting Exoplanet Survey Satellite (TESS, Ricker et al. 2014). The first, Sector 6, had a 30-minute cadence and was observed between 2018 December 15 and 2019 January 06. Lomb-Scargle period analysis (Lomb 1976; Scargle 1982) revealed strong evidence of periodicity at 3.941 ± 0.010 hours, which was attributed to be the orbital period of the system by Schwope et al. (2022). It was later again observed in Sector 33 with a 2-minute cadence between 2020 December 18 and 2021 January 13. A periodogram of this obser-

vation revealed maximum power at 24.37 minutes, possibly the WD rotation period, with no indication of the 3.941 hour periodicity found in the Sector 6 observation. Additional ground-based photometric observations conducted using the 1.0m telescope at the South African Astronomical Observatory (SAAO), however, did not find any of the periods detected in the *TESS* observations, and instead revealed strong evidence of a 34.7-minute period, possibly indicative of an IP classification.

One of the fundamental properties of a CV is the periodicities, both orbital and WD-spin, found in such a system. Therefore, the optical time-resolved spectroscopic and photometric observations presented in this paper were obtained to put better constraints on the nature of this system, with determining these periodicities as the primary question to be answered. The time-resolved spectroscopic observations are especially revealing, as this is the first time that such observations are published for this system. To further determine the nature of SRGt 062340, a parallel paper by Cúneo et al. (2026) reports on XMM-Newton and eROSITA X-ray observations. In this paper, the results from Cúneo et al. (2026) will also be used to establish the most likely periodicities found in this optical study. This paper is structured as follows, Section 2 gives an overview of the spectroscopic and photometric observations that were obtained, as well as the archival photometric observations used, while Section 3 gives a description of how the data was reduced and analysed. In Section 4 the results are discussed, and in Section 5 the conclusions of these observations are made. The appendix consists of three sections. The first, appendix A, are the observing logs of all the SAAO spectroscopic and photometric observations analysed. In appendix B and appendix C has additional plots and tables for the spectroscopic and photometric results, respectively.

2. Observations

2.1. SAAO 1.9m *SpUpNIC* spectroscopy

Long-slit spectroscopic observations of SRGt 062340 using the SpUpNIC spectrograph (Crause et al. 2016) on the SAAO 1.9m telescope were conducted on several epochs between 2021 February and 2021 March. All observations were made using grating 4; however, two different grating angles, 5.50° and 4.20° , were used. The resolution of the spectra were determined by measuring the FWHM of several wavelength calibrated arc lamp spectra and is $\sim 2.3 \text{ \AA}$ for both configurations. A summary of these observations is given in Table A.1 in the appendix.

Standard IRAF (Tody 1986) procedures were followed in the reduction of these observations. On some nights bias and flat field images were not taken, and the calibration images from the nearest nights where those were taken was then used. Due to the shifting orientation of the spectrograph through the course of an observation, that might cause flexure in the instrumentation, calibration arc images were taken throughout the observations. The science images that were taken between two arcs were wavelength calibrated by an arc image that is the median combination of the arcs taken before and after the given science images. Spectrophotometric standard star observations were also carried out on several nights which were used to flux calibrate the observations.

2.2. SALT HRS

SALT HRS observations were conducted on several epochs from 2023 November - 2024 April in low-resolution mode ($R \sim 15000$) where, for each epoch, either two or four spectra were

¹ <https://vsx.aavso.org/index.php?view=detail.top&oid=477558>

² <https://arxiv.org/abs/astro-ph/0004053v2>

obtained. A summary of these observations is given in Table A.3. HRS is a dual-beam fibre-fed échelle spectrograph with a wavelength coverage of $\lambda \sim 3800\text{-}8900\text{\AA}$, where the ‘blue arm’ covers $\lambda \sim 3800\text{-}5500\text{\AA}$, and the ‘red arm’ covering $\lambda \sim 5500\text{-}8900\text{\AA}$, respectively. Initial reductions, flat field and bias corrections, were performed using the PySALT package (Crawford et al. 2010), while the spectrum was extracted using the HRS pipeline (Kniazev et al. 2016), which incorporates MIDAS (Baner et al. 1983) routines.

2.3. SAAO photometry

Optical photometric observations were carried out for SRGt 062340 on 16 epochs from 2020 November 1 to 2021 March 2. Table A.2 gives a summary of all the photometric observations. The observations were taken using the two SAAO 1.0 metre telescopes, with most of the observations being obtained with a clear filter (in white light); however, some observations were also obtained in g' and r' . Those observations taken on the nights of 2020 November 2 and 3, as well as 2020 December 3 and 4 were of poor quality and were excluded from any analysis. The adaptive elliptical aperture photometry (TEAPhot, Bowman & Holdsworth 2019) package was used to perform differential photometry, with UCAC2 20781392 (V=12.08 mag) as a comparison star. Lomb-Scargle techniques from Astropy (Astropy Collaboration et al. 2022) as well as the general tools for astronomical time series in python (Gatspy, VanderPlas & Ivezić 2015) code was used to perform period analysis of the SRGt 062340 light curves (using the LombScargleFast model).

2.4. TESS photometry

SRGt 062340 was observed in three sectors³. The first at 30-minute cadence in Sector 6 from JD 2458468.2742170 (2018 December 15) to JD 2458490.0452274 (2019 January 06). It was then observed at a higher 2-minute cadence in Sector 33 from JD 2459201.7324158 (2020 December 18) to JD 2459227.5723964 (2021 January 13) and Sector 87 from JD 2460663.0380630 (2024 December 18) to JD 2460689.9405712 (2025 January 14).

2.5. Archival photometry

Additional archival long-term photometric observations from the Catalina Real-Time Transient Survey⁴ (CRTS, Drake et al. 2009) was found that spans from JD 2453610.74097 (2005 August 28) to JD 2456422.41004 (2013 May 9). Further archival data was found from the All-Sky Automated Survey for Supernovae⁵ (ASAS-SN, Kochanek et al. 2017) that spans from HJD 2456596.011616 (2013 October 30) to HJD 2460815.46763 (2025 May 19). Figure 1 shows the combined archival CRTS and ASAS-SN light curve, with the epochs of the observations reported in this paper highlighted. The inset plot focuses on the epoch of the SAAO photometric observations, and show variability in the light curve during this observing run.

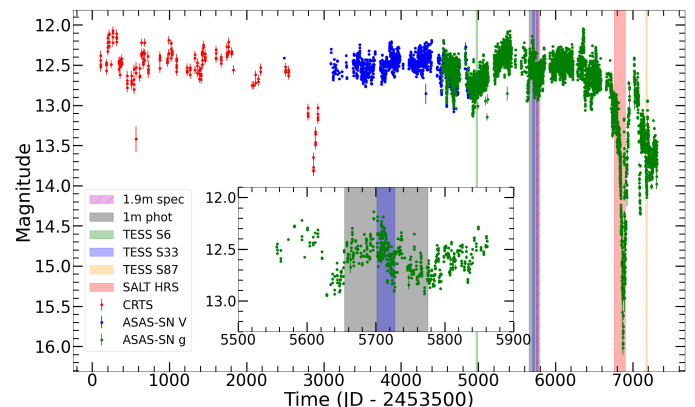


Fig. 1. CRTS V-band (Catalina ID 3027043037227) and ASAS-SN light curve of SRGt 062340 taken using g and V filters. Superimposed are the photometric and spectroscopic observations reported on in this study. Refer to the appendix and text for more detail on observation epochs. The inset plot has the same axes as the main plot, and focuses on the epochs of photometric TESS and SAAO observations. The magnitude ranges from 12.14 - 12.93 during the SAAO photometry campaign

3. Analysis

3.1. SAAO 1.9m long-slit spectroscopy

3.1.1. Spectral line measurements

Figure 2 shows the median combined and flux calibrated spectrum from the 2021 February 2 SpUpNIC observation, as a typical example, which shows a continuum that is rising to higher intensities towards the blue. The spectrum shows very prominent, narrow and single peaked emission lines, centred on shallow broad absorption troughs, for the Balmer $H\beta$ and $H\gamma$ lines. Other weaker emission lines are seen, such as $He\text{ II } \lambda 4686$ together with the Bowen blend around $\lambda 4640$, as well as the $He\text{ I } \lambda 4471, \lambda 4921$ lines and possible $C\text{ II } \lambda 4267$. Figure 6 in (Cúneo et al. 2026) shows the SED of the system, from which we can conclude that the absorption lines likely emanate from an optically thick accretion disc, and not from the photosphere of the WD. Donor star spectral features are usually, if they are present, seen at longer wavelengths than that covered in these observations, and hence no spectral features that could be associated with the donor star are seen in the spectrum. The spectroscopic analysis of the SpUpNIC observations will focus on the $H\beta$, $H\gamma$ and $He\text{ II } \lambda 4686$, being the strongest lines. Figure B.1 show trailed spectra of $H\beta$ and $H\gamma$ for the February 27 observation, the longest continuous observation in our dataset. The emission lines show little change, by eye at least, in either intensity, structure or position with time, although the line centroids appear slightly shifted towards longer wavelengths compared to the respective rest wavelengths (vertical dashed lines).

Broad absorption lines are seen as the broad dark regions adjacent to the emission lines, and is most prominent for $H\gamma$. The strength of this absorption does not appear to be constant, with sporadic increases (darker bands) in absorption strength, appearing in both the Balmer lines simultaneously; however, it is slightly more pronounced for $H\beta$. The duration and frequency of these sporadic increases in absorption is also not constant. There is no indication in any of the trailed spectra of an emission-line ‘S-wave’ that could be associated with the bright spot on an accretion disc, which might be due to insufficient resolution

³ <https://mast.stsci.edu/portal/Mashup/Clients/Mast/Portal.html>

⁴ <http://crtsn.caltech.edu/>

⁵ <https://asas-sn.osu.edu/>

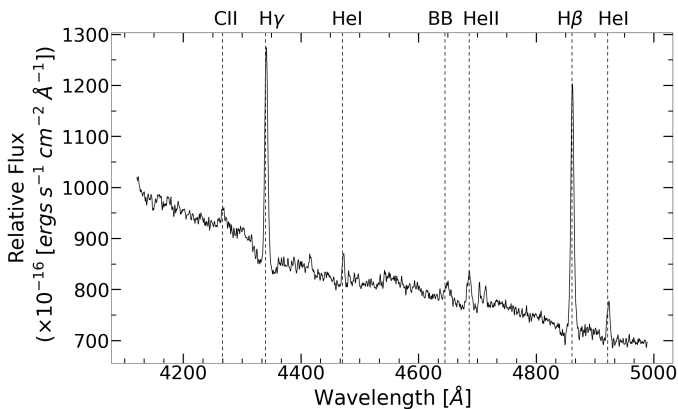


Fig. 2. Median combined flux calibrated spectrum ranging from 4100Å–5000Å of the nine observations made on 2021 February 2. ‘BB’ indicates the Bowen fluorescence blend.

of the spectra coupled with the likely low inclination, as seems likely from the line morphology.

To study both the emission and absorption components of the Balmer lines, the Python package `lmfit` (Newville et al. 2016) was used to fit three components, an emission, an absorption, and one to model the continuum, to the spectra. Various different profiles were considered to model each component of the spectral line. It was found that a combination of two Gaussians, one for emission and one for absorption, together with a linear model for the continuum, had the lowest reduced χ^2 value. This was subsequently chosen to model the spectral lines. An additional Gaussian component had to be added to the $H\beta$ model to take into account the effect of the $He\text{I } \lambda 4921$ line. $He\text{II } \lambda 4686$ only shows an emission component and a Gaussian profile was fitted to it, as well as another Gaussian for the Bowen blend, bluewards of $He\text{II}$, together with a linear fit to the continuum. An illustration of the `lmfit` modelling to $H\beta$ and Hy is shown in Figure 3.

Using these model fits, parameters such as the central line positions, flux and FWHM were measured for the respective spectral lines for all the observations. Table B.1 gives a summary of the averaged FWHM for the $H\beta$, $He\text{II } \lambda 4686$ and Hy emission lines per night, while Table B.2 shows the averaged $H\beta$ and Hy absorption line measurements. The emission lines are narrow, with average widths of 316 ± 8 km s $^{-1}$, 401 ± 29 km s $^{-1}$, and 317 ± 9 km s $^{-1}$ for $H\beta$, $He\text{II } \lambda 4686$, and Hy , respectively. The widths of the lines do vary, with a difference between maximum and minimum width for $H\beta$ of 34 km s $^{-1}$, 20 km s $^{-1}$ for $He\text{II } \lambda 4686$ and 75 km s $^{-1}$ for Hy . The Balmer absorption lines are very broad and shallow which, together with the bright emission cores, makes it difficult in determining the line parameters for the absorption components and therefore the results should be taken with caution. This is especially true for $H\beta$, as the absorption line is broader and shallower as that of Hy .

3.1.2. Spectroscopic orbital period

Lomb-Scargle period analyses were done on the $H\beta$ and Hy emission line radial velocity measurements to find the spectroscopic period of the system. All the data apart from that obtained on 2021 February 2 was used for the analysis, as those observations were taken at a different exposure time from the rest (Table A.1). The data was further divided into two sets to systematically study the period and see whether there is any change in the periodic behaviour on a scale of weeks. Data Set 1 (DS1) contains

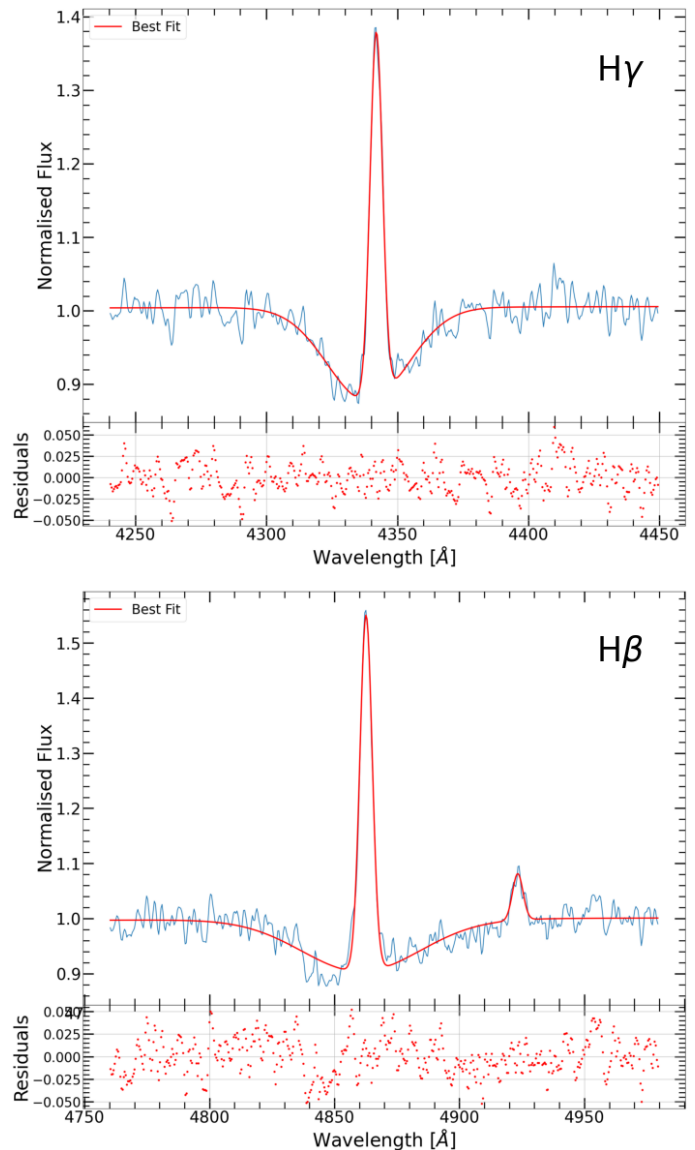


Fig. 3. `lmfit` Hy (top) and $H\beta$ (bottom) modelling for an observation obtained on 2021 February 26, where the bottom panels of each line shows the respective residuals of the fit.

the data obtained from the 2021 February 26 – 2021 March 2 observations, while Data Set 2 (DS2) contains the data from the 2021 March 17 – 2021 March 22 observations. The respective periods found are listed in Table 1. The Lomb-Scargle power spectrum for $H\beta$ DS1 has the most power at $P_{H\beta, DS1} = 3.650 \pm 0.040$ hours, while for DS2 it is at $P_{H\beta, DS2} = 4.341 \pm 0.050$ hours. The difference in the two separate datasets for $H\beta$ corresponds to the 1 cycle/day alias as a result of the data sampling. The periods obtained for the two datasets of Hy are almost identical, with $P_{Hy, DS1} = 3.646 \pm 0.423$ hours and $P_{Hy, DS2} = 3.659 \pm 0.348$ hours, respectively.

To get a better constraint on the spectroscopic orbital period, power spectra were produced by combining all (i.e. both datasets) of the $H\beta$ and Hy emission radial velocities, respectively. Figure 4 show both the $H\beta$ (top panel) and Hy (second panel) power spectra, where the inset plots show zoomed in regions around the identified periods. It is unclear why so much power is seen at low frequencies in the combined Hy power spectrum, which has its strongest peak at a frequency that cor-

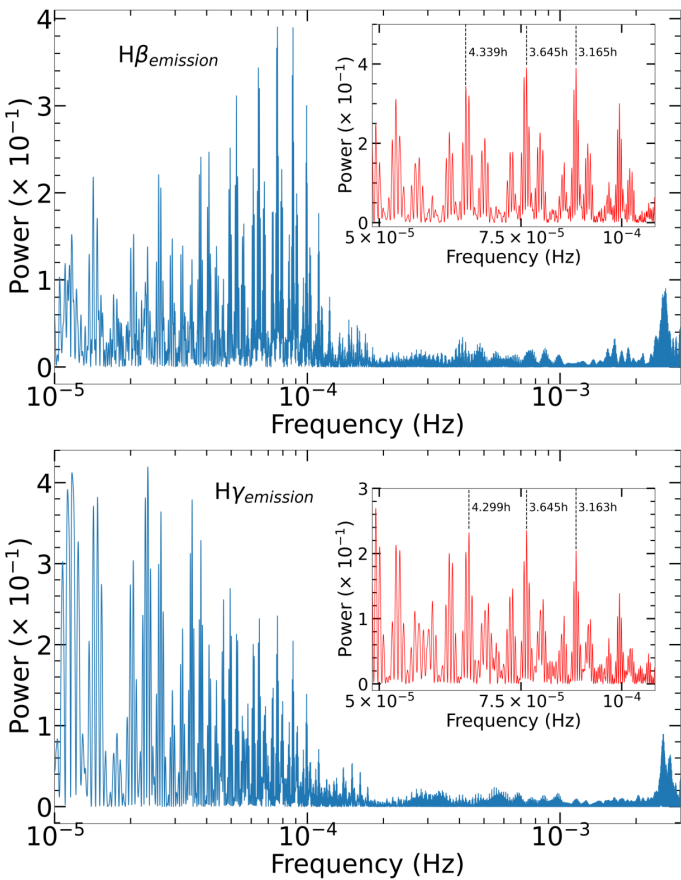


Fig. 4. Power spectra obtained using the H β (top) and H γ (bottom) emission line radial velocity measurements using all the datasets. The inset shows the frequency range of the suspected orbital period of the system. It is found that all indicated periods are one-day aliases.

Table 1. Spectroscopic periods

	Data	H β Period (h)	H γ Period (h)
Emission	Data Set 1	3.650 ± 0.040	3.646 ± 0.423
	Data Set 2	4.341 ± 0.050	3.659 ± 0.348
	All	3.645 ± 0.006	3.645 ± 0.006
Absorption	Data Set 1	1.137 ± 0.041	3.178 ± 0.320
	Data Set 2	0.173 ± 0.001	5.338 ± 0.748
	All	0.261 ± 0.001	3.677 ± 0.055

Data Set 1: 2021 February 26, 27, March 2

Data Set 2: 2021 March 17, 18, 19, 20, 21, 22

All: All data (i.e. Data Set 1 + Data Set 2)

responds to a period of 11.86 hours. This is surprising given that the H γ DS1 and DS2 dominant periods were both ~ 3.65 hours. Using the DS1 and DS2 periods as a guide, as well as the periods found in the H β power spectra, only periods below 4.5 hours were considered as probable orbital periods. Several strong peaks are seen for both H β and H γ in the ~ 0.05 - 0.10 mHz frequency range, which are due to aliasing. The strongest peak in H β is seen at 0.0762 mHz, corresponding to a period of 3.645 hours. This is also seen for H γ , from which we conclude that this is the orbital period.

A similar analysis was attempted for the H β and H γ absorption radial velocity measurements, with the results summarized in Table 1 and Figure 5. It is immediately clear that for the H β

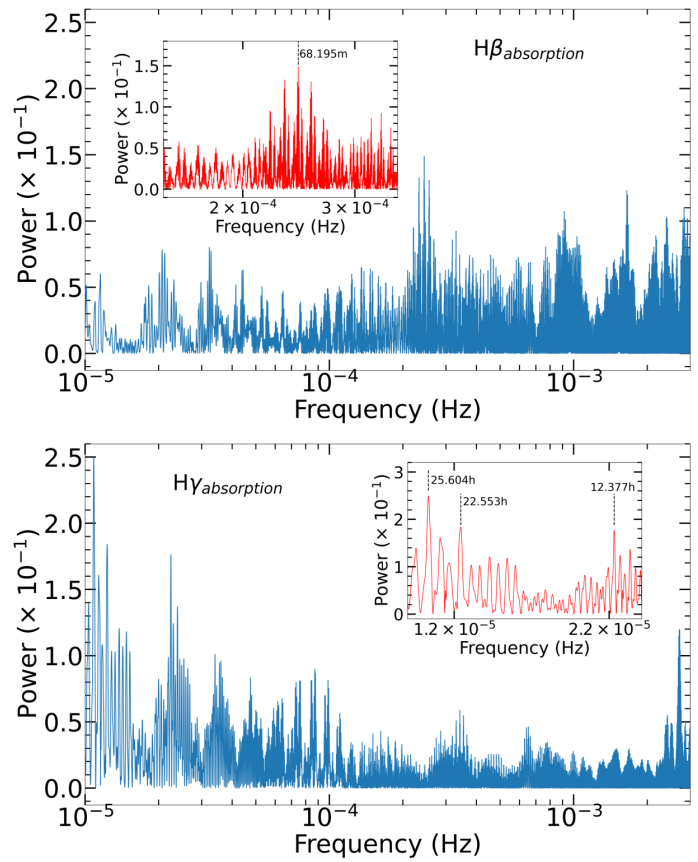


Fig. 5. Power spectra obtained using the H β (top) and H γ (bottom) absorption line radial velocity measurements using all the datasets. The inset plot shows the frequency range of the suspected orbital period of the system. It is found that all indicated periods are one-day aliases.

absorption component, there is no clear indication of the orbital period, or indeed any period above the noise threshold, apart for a $5-\sigma$ signal at 68.195 minutes (and its corresponding aliases). This is likely because the H β absorption lines are much shallower and broader than in the case of H γ , and therefore more difficult to fit and obtain a reliable centroid. For the stronger H γ absorption, however, the combination of both datasets, i.e. ‘All’, agrees within the uncertainty with the period found from the emission line radial velocities, while the Data Set 1 results is a 1-cycle per day alias of this period (Table 1).

Figure C.4 shows log-log power spectra of the Balmer emission line radial velocities, where the positions of the spectroscopic orbital frequency, Ω (obtained in Section 3.1.2), as well as the possible spin frequency of the WD, ω , are also shown (see Section 3.3). Clearly there is no evidence of significant power in the radial velocities at the photometrically derived spin frequency. The power excess, or ‘arching effect’ at $\nu < 10^{-4}$ Hz, seen in the bottom panel of Figure C.4 is due to data gaps in the SAAO photometry.

3.1.3. Orbital ephemeris

The orbital phases for each observation were determined using the spectroscopic orbital period, $P_{orb} = 3.645$ h. This was accomplished by first arbitrarily assigning the BJD of the first observation taken on 2021 February 26 as phase 0, and then subsequently determining the phase of all the other observations from this point of reference. A sine function of the form $K \sin(2\pi(f t + \phi)) + \gamma$, where K is the amplitude, ϕ the phase shift,

Table 2. Phase-folded parameters

Line	K (km s ⁻¹)	γ (km s ⁻¹)	ϕ
Emission			
H β	14.05 \pm 0.67	37.34 \pm 0.47	0.98 \pm 0.09
H γ	15.10 \pm 1.30	38.46 \pm 0.91	1.05 \pm 0.17
He II λ 4686	15.59 \pm 2.71	47.09 \pm 2.06	0.65 \pm 0.36
Absorption			
H β	67.52 \pm 14.99	538.90 \pm 11.26	0.77 \pm 0.44
H γ	47.94 \pm 12.97	27.36 \pm 9.35	0.74 \pm 0.52

and γ the systemic velocity of the system, was fitted to the H β radial velocities to determine the phase shift that was needed to determine the BJD T_0 , where the system shows a radial velocity exactly midway between maximum and minimum (i.e. the point of inferior conjunction of the companion star).

The fit revealed a very low amplitude of $K = 14.05 \pm 0.67$ km s⁻¹ and a systemic velocity of $\gamma = 37.34 \pm 0.47$ km s⁻¹. Applying the phase shift, determined from the sine function, the true BJD T_0 was derived. The ephemeris of SRGt 062340, as determined from the H β radial velocity measurements, is therefore

$$T_0 = 2459273.078516(28) + 0.151875(25) \times E.$$

Figure 6 shows the resulting sine fit of the radial velocity measurements to the phase-folded H β emission and absorption lines, together with the residuals of the fit. Figure B.2 in the appendix show the fit to the H γ emission and absorption lines, as well as He II λ 4686 emission line. The parameters for these fits are presented in Table 2. Despite the good quality of the spectral fits, with reduced $\chi^2 \approx 1$, there is a lot of scatter in the radial velocity measurements that are larger than the uncertainties in the individual measurements. A possible explanation for this could be that using the generic templates in the lmfit modelling is not sufficient for this system, and employing physically self-consistent accretion disc line profiles might, in principle, improve the stability of the radial velocity measurements. Given the available data, we however assume that the overall radial velocity behaviour is nonetheless reliably represented by our analysis. We therefore focus on the mean radial velocity behaviour, which we assume to be robust. Figure 7 shows the phase-folded trailed spectra of H β and H γ in velocity space. The system has a small velocity amplitude; however, the orbital modulation is evident in the phase-folded trailed spectra. While it is not immediately clear as to why some data points appear to be outliers, one possible interpretation could be that they are due to flaring events in the system which might introduce peculiar velocities.

3.1.4. Phase-folded radial velocities

From Table 2 it is seen that all of the emission line phase values agree with each other within the uncertainties of the measurements. The radial velocity amplitudes for the two Balmer and He II λ 4686 emission lines are all similar, with $K \sim 14.5$ km s⁻¹, although the He II plot has a lot more scatter, being a weaker line (see Figure B.2) with consequently larger velocity uncertainties.

Despite the larger uncertainties associated with the absorption line measurements, compared to the emission lines, it is still instructive to compare the phase-folded absorption line radial velocities to those of the respective emission lines. As expected, the absorption line measurements show a lot more scatter compared to the emission lines. However, an orbital modulation in

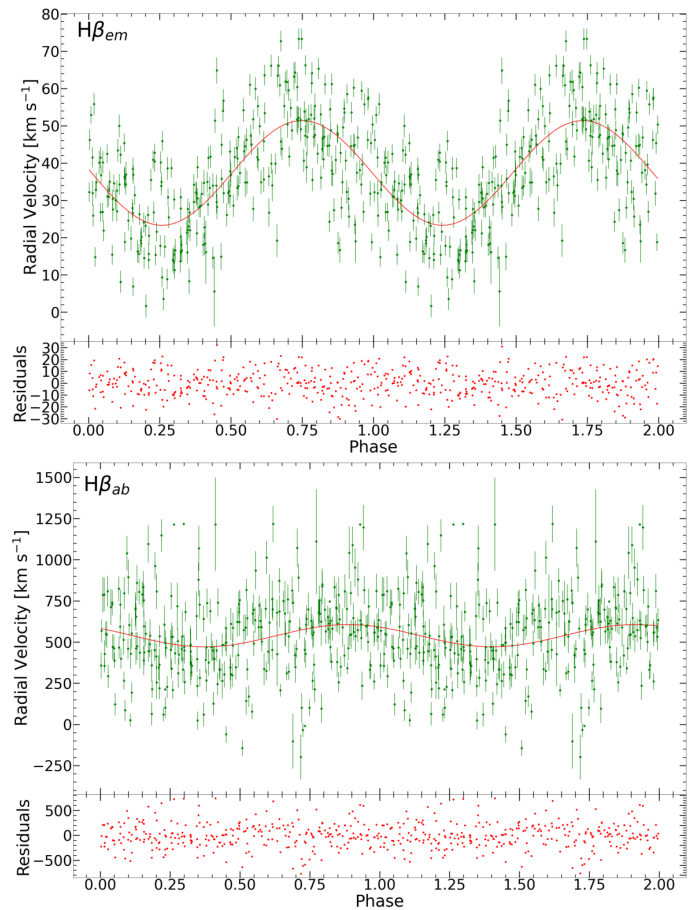


Fig. 6. H β emission (top) and absorption (lower) line radial velocities phase-folded on the 3.645-hour period. The fitted sine functions, with the parameters in Table 2, are also shown, with the residuals in the lower panels of each plot.

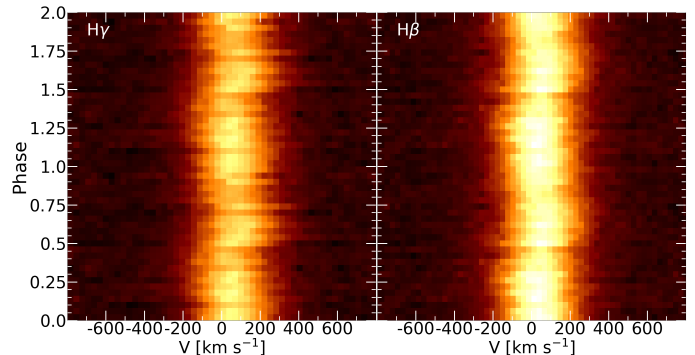


Fig. 7. Trailed spectra phase-folded on the best (H β) spectroscopic orbital period (3.645h). Left is H γ and right H β .

the absorption lines is still observed and it is only slightly out of phase with the emission components ($\Delta\phi \sim 0.2$, see Table 2), though the uncertainties are large. One peculiarity is that of the H γ absorption line has a γ velocity (i.e. systemic) similar to that found for all the emission lines, whereas the H β line has a substantial γ velocity of ~ 540 km s⁻¹. This could be attributed to poor modelling of the H β absorption component, which is due to the shallow and broad nature of the line with a superposed strong emission line in its core. Thus, the H β γ velocity should not be considered in the rest of the analysis.

3.2. SALT HRS

SALT HRS observations were obtained with the aim of determining whether the Balmer emission lines were truly a simple Gaussian, as the SAAO 1.9m observations suggested, or whether the emission lines have a more complex, non-Gaussian, morphology. Figure 8 shows zoomed-in regions for $H\alpha$, $He\text{i } \lambda 5876$, $H\beta$, and $H\gamma$ of the four spectra that were obtained on 2024 January 13. Even though moving 1D box kernel smoothing was applied to all spectra (with sizes 3, 7, 4, and 11 for $H\alpha$, $He\text{i } \lambda 5876$, $H\beta$, and $H\gamma$, respectively (due to the different resolution at different wavelengths)), it is evident, for $H\alpha$ at least, that the emission line does not have a strict Gaussian profile, having double peaks. These peaks seem to be changing, with both blue and red peaks being equally prominent in the first observation and the blue peak becoming more prominent in subsequent spectra. Even though the double-peak structure is not strong, it is an indication of a possible disc in the system that is seen at a low inclination angle. It is not clear whether double peaks can be seen for $H\beta$ or $H\gamma$; however, the emission line profile for all three Balmer lines does seem to be a non-uniform Gaussian, with an extended red-wing, which could indicate a high velocity component. $He\text{i } \lambda 5876$ also suffer from high noise levels; however, the profile appear to be Gaussian. Due to the high noise level, it is difficult to determine whether multiple components are present in the $He\text{i } \lambda 5876$ emission, but it does appear likely. There are indications of blueshifted absorption in the second and third spectra of Figure 8, especially for $He\text{i } \lambda 5876$, which could indicate the presence of a P-Cygni profile caused by a disc wind (e.g. Cúneo et al. 2023).

The question now arises of whether the change seen in the morphology of the $H\alpha$ emission line is phase dependent. To answer this, `lmfit` modelling to each spectrum was done using a double Lorentzian profile (which gave a better reduced χ^2 fit to the majority of the spectra compared to a double Gaussian model), to fit a profile to the blue and red components, respectively. The radial velocity of both components was determined from this fit, and is captured in Table B.3, together with the HJD and phase of the respective observations. The phase of each HRS observation was determined using the orbital ephemeris as stated in Section 3.1.3. The top panel of Figure 9 shows the radial velocities of the blue and red components for all 48 HRS spectra, while the bottom panel of the figure shows the difference in wavelength between the two components. The radial velocities seem to roughly follow a sinusoidal pattern of very low amplitude (few tens of km s^{-1}), indicative of motion about the centre of mass in the system. However, the bottom panel of Figure 9 shows a random scatter, and hence no clear phase-dependent behaviour in the morphology of the $H\alpha$ emission line.

Using a phase bin of $\phi=0.1$, spectra were phase-binned together (by median combining all the spectra that fall within a given bin using `IRAF`) to determine whether any underlying phase-dependant morphology could be seen in the $H\alpha$ emission line. However, no phase-dependant morphology in the line was seen. As with the individual spectra, `lmfit` was used to model the binned spectra, which is summarized in Table B.4.

3.3. SAAO photometry

3.3.1. Light curves

Strong short timescale variability (on timescales of minutes) is seen in all the light curves, with the frequency and amplitude of peaks and dips varying from epoch to epoch, with no apparent

repeating pattern or frequency (confirmed in Section 3.3.2 from power spectra). Figure C.1 in the appendix show the optical light curves for each night, together with the respective Lomb-Scargle power spectrum. The light curves show the normalized differential magnitude, where the magnitude of the comparison star was subtracted from the target star, giving the differential magnitude, after which the data were normalized by subtracting the average of this differential magnitude from each data entry (with negative values being brighter than positive values). Dips generally appear to have a similar steep slope during rise and fall. Phase folding light curves on the spectroscopic orbital period (i.e. 3.645 hours) reveal that the variability does not appear to be phase dependant either, and show strong stochastic variability from orbit to orbit. Such stochastic variations, at relatively high amplitudes, are quite common in CVs and indeed many IPs (e.g. for TX Col, see Fig. 10 in Buckley & Tuohy (1989)).

3.3.2. Power spectra

Table C.1 lists all the strongest peaks found from the Lomb-Scargle period analysis of each observation epoch and shows that no single coherent period is common to all the individual observations. The uncertainties in the periods found from the Lomb-Scargle power spectra were obtained using bootstrapping techniques, similar to what was used by Zurek et al. (2009). For each light curve, 10,000 synthetic light curves were generated. A Lomb-Scargle period search was again performed for each of those, finding the best period. The uncertainty in the period was then taken as the standard deviation of the best periods found of the 10,000 synthetic light curves. In Table 3 observations from different epochs were grouped together in the hope that the longer observation baseline will put a better constraint on the photometric periods. The grouping of data was largely determined from temporal considerations, the details are given in the footnote of Table 3. There is again no consistent period found between the datasets and the uncertainties are large, with the exception of Data Set 6 (DS6), namely all the combined clear filter data. The larger baseline of this dataset gives the best resolution power spectra. Apart from the region of lowest frequencies near the orbital period, a strong peak was found at a much higher frequency of $0.66920 \pm 0.0036 \text{ mHz}$ (or $P = 24.905 \pm 0.065 \text{ minutes}$). This is very close to two periods identified in the *TESS* Sector 33 (high cadence) data power spectra, namely at 24.37 and 25.20 min, identified by Schwope et al. (2022) as a possible spin period. This peak in the power spectrum might be interpreted as the likely spin frequency of the WD, ω .

Figure 10 shows the resulting power spectrum for all the clear filter combined data (DS6). There is a strong indication of a peak at the rotation frequency, ω , while power is seen at lower frequencies. The spectroscopic orbital frequency, Ω (associated with $P_{\text{orb}} = 3.645 \text{ hours}$), is indicated as well, but does not coincide with the strongest peak at low frequencies (which is at $\sim 5.022 \text{ hours}$). The inset shows a region zoomed-in on 0.4–0.8 mHz, showing the spin frequency. Figure 10 also shows a lot of aliasing, which is due to the irregular intervals between observations within the ~ 17 weeks of observations.

Figure 11 shows the clear filter observations phase-folded on the spin and orbital periods, where the observations were binned in $\phi=0.04$ bins. Modulation on the spin period is clearly seen.

To investigate whether ω is significant and a stable period, the data was divided into three groups and subjected to period analysis. Figure C.3 shows the resulting power spectra of com-

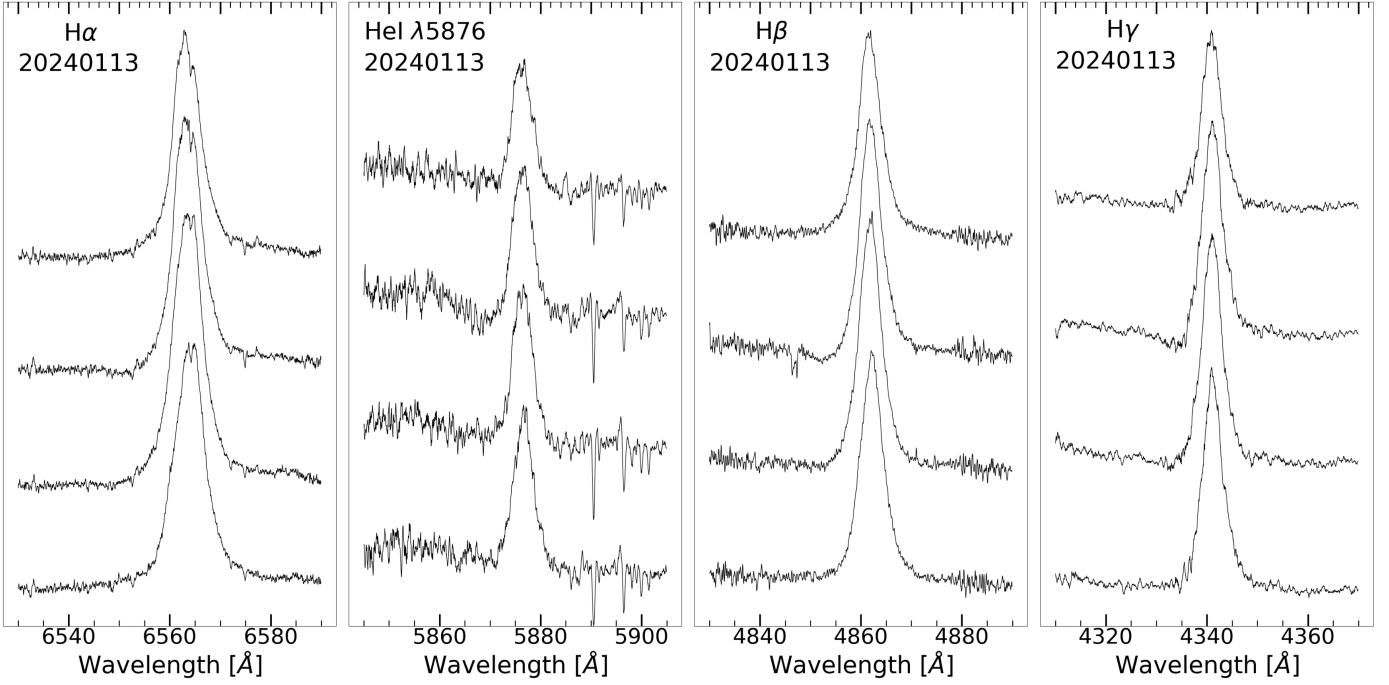


Fig. 8. 2024 January 13 continuum subtracted normalized SALT HRS stacked spectra, focusing on the Balmer emission lines as well as He I $\lambda 5876$. All the spectra were smoothed by a moving 1D box kernel of size 3, 7, 4, and 11 for H α , He I $\lambda 5876$, H β , and H γ , respectively. Each spectrum is a 600-second exposure, with the first spectrum being the first from the bottom and the last spectrum obtained at the top. The absorption features seen at around 5890Å and 5896Å in the He I plot are from telluric lines. Note, the absorption to the blue in the third spectrum of the emission lines. The offset of the stacked spectra were 0.0023, 0.001, 0.0025, and 0.007 for H α , He I $\lambda 5876$, H β , and H γ , respectively.

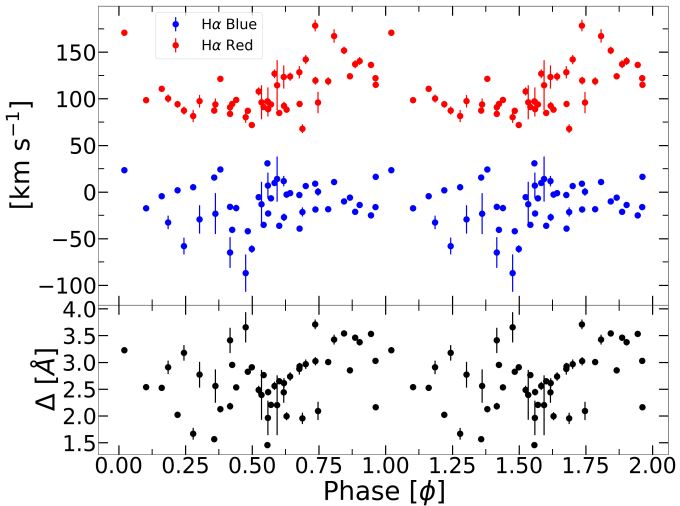


Fig. 9. Radial velocity measurements of the SALT HRS observations for both the blue and red components of H α , phase-folded on the suspected orbital period of $P_{\text{orb}} = 3.645$ hours (top panel). Difference in wavelength between the red and blue components (bottom panel).

bining the observations obtained in 2020 November, 2021 January, and 2021 February. ω is also indicated in the respective plots and show that some power, and at roughly the same intensity, is seen in all three groupings at this frequency. However, the aliasing is quite complex, and it is clear that there are significant changes in the power spectra and where the maximum power is seen in all three groupings. This indicates changes on timescales of weeks, or shorter, which could imply that SRGt 062340 is subject to QPOs, similar to what has been seen in other systems,

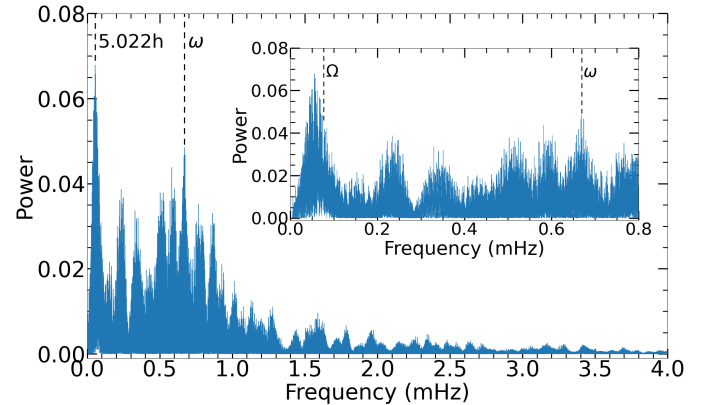


Fig. 10. Lomb-Scargle power spectrum using all the clear filter photometric observations. The frequency of the strongest peak coincides with a period of 5.022 hours. The probable spin frequency of the WD is indicated by the dashed line labelled ω . The inset plot focuses on the region 0.0 - 0.8 mHz and show the position of the spectroscopic orbital period, Ω , and the probable spin frequency.

such as the IP, TX Col (Littlefield et al. 2021). A more definitive answer to the question of whether there's a coherent spin period needs time series X-ray observation, which is reported in Cúneo et al. (2026).

3.4. TESS photometry

Schwöpe et al. (2022) report on the results of two *TESS* observations, observed in Sector 6 and Sector 33. In this section some of those results are reproduced, and we report new *TESS* photom-

Table 3. Differential photometry periods when combining data sets

Data	Filter	Period (hours)	Period (min)
Data Set 1	clear	0.5728 ± 0.0023	34.3 ± 0.1
Data Set 2	clear	5.0183 ± 0.0047	301.2 ± 0.3
Data Set 3	clear	1.3355 ± 0.0029	80.0 ± 0.2
Data Set 4	clear	3.3274 ± 0.0185	202.0 ± 1.1
Data Set 5	g'	3.9847 ± 0.0022	238.9 ± 0.1
Data Set 6	clear	0.4151 ± 0.0011	24.905 ± 0.065

Data Set (DS) 1: 2020 November 27, 28, 29

DS 2: 2021 January 4, 13, 20

DS 3: 2021 February 1, 2

DS 4: 2021 February 26, 27

DS 5: 2021 February 27, March 2

DS 6: All clear observations

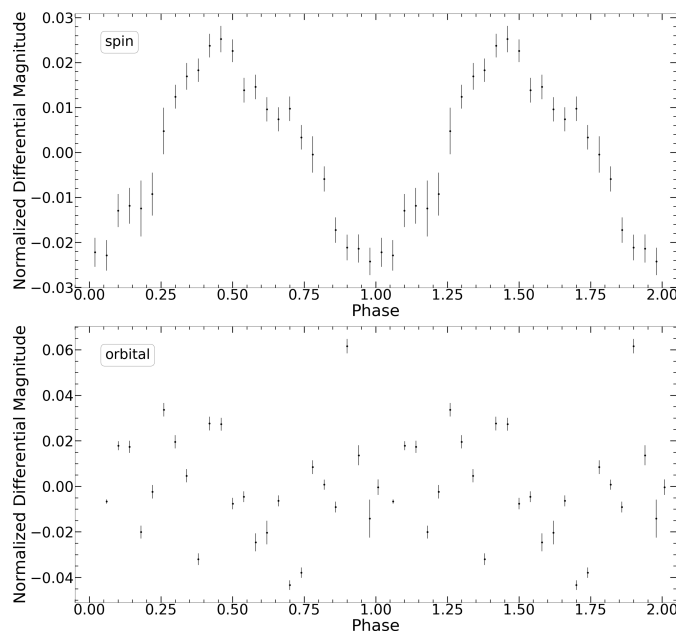


Fig. 11. Binned phase-folded light curves of all the clear filter observations. Top panel is folded on the spin period, 24.905 minutes, while the bottom panel is folded on the 3.645-hour orbital period.

etry from Sector 87 at 2-minute cadence. The low cadence 30-minute Sector 6 light curves were obtained from the *TESS* full-frame images, while the higher cadence 2-minute Sector 33 light curves were obtained from Pre-search Data Conditioning (PDCSAP) fluxes. Full details of the reduction of the two datasets are outlined in Schwope et al. (2022); however, it should be mentioned that Littlefield et al. (2021) points out that using *TESS* PDCSAP flux light curve data can suppress slow stochastic variability of true astrophysical origin. Therefore, here we reproduce the data from Sector 6 in the same manner as in Schwope et al. (2022), but for Sector 33 and 87 we use the *TESS* light curve constructed from the *TESS* Simple Aperture Photometry (SAP) flux. All *TESS* data were downloaded using the *Lightkurve* package⁶ (Lightkurve Collaboration et al. 2018), which was also used to remove the cosmic rays. All data points with quality flag greater than 0 were excluded.

The main strength of *TESS* comes from its exceptional relative photometry. However, in order to convert it to absolute photometry, other simultaneous ground-based data is required. For

this purpose we use quasi-simultaneous ASAS-SN *g*-band data (Shappee et al. 2014; Kochanek et al. 2017) similarly to Scaringi et al. (2012a) and Veresvarska et al. (2024a). With the *g*-band central wavelength of 475 nm and 140 nm width, the band is partially overlapping with *TESS* passband (600 – 1000 nm). Assuming no colour-term variations, the data obtained from the ASAS-SN webpage can be used to convert the *TESS* flux in $\text{e}^{-\text{s}} \text{ s}^{-1}$ to ASAS-SN *g*-band flux in mJy. We do this by adopting the following linear relation between the fluxes $F_{\text{ASAS-SN}} [\text{mJy}] = A \times F_{\text{TESS}} [\text{e}^{-\text{s}} \text{ s}^{-1}] + C$. The fully converted *TESS* data with the used ASAS-SN *g*-band light curve is shown in Figure C.2. The dashed grey line in the middle panel showing *TESS* Sector 33 data denotes a cut-off point, after which the light curve is no longer stationary. As such, the data beyond BJD-245700 ~ 2225 is not used in this work.

In order to examine any potential periodic signals in *TESS* data, we compute the Lomb-Scargle periodogram of each separate Sector. The zoom in of this is shown in Figure 12. As reported in Schwope et al. (2022), Sector 6 shows a distinct coherent period at 3.941 hours and its first harmonic (marked as P_{PSH} and $2P_{PSH}$ in Figure 12). Both Sectors 33 and 87 show no evidence of this signal. Sector 33 however shows a potential signal at ~32 hours. The phase-folded light curve on this period, binned into 50 phase bins, is shown in the inset plot of the middle panel of Figure 12. The newest Sector 87 shows no sign of any periodic signals.

A time-averaged power spectrum (TPS) is computed for Sectors 33 and 87 of *TESS* data and shown in Figure 13. The TPS is constructed by separating the light curve of an individual Sector into 4-day segments. A segment of 4 days is chosen to maximise the number of segments in each Sector whilst minimising data gaps in each segment. A Lomb-Scargle periodogram of each of the segments is then computed, before the individual power spectral densities (PSDs) are averaged together and binned onto a coarser frequency bin ($N_{\text{bins}} = 90$). The TPS allows for an easier examination of the broad-band shape of the power spectrum and increased signal-to-noise ratio that facilitates fitting the broad-band components of the TPS. To fit the TPS, we use Lorentzians and a Poisson noise component, similarly to Veresvarska et al. (2024b):

$$P_{\nu} = \sum_{i=0}^{N=2} P_L(r_i, \Delta_i, \nu_{0,i}, \nu) + A,$$

where A represents the Poisson noise level and $P_L(\nu)$ stands for the RMS normalized power of each individual Lorentzian, such that

$$P_L(\nu) = \frac{r^2 \Delta}{\pi} \frac{1}{\Delta^2 + (\nu - \nu_0)^2},$$

with Δ corresponding to the half width half maximum (HWHM) and r a normalization factor proportional to the integrated fractional rms. ν_0 is the centroid frequency of the Lorentzian, with the frequency of the peak of the Lorentzian being defined as

$\nu_{\text{max}} = \sqrt{\nu_0^2 + \Delta^2}$ for $\nu_0 > 0$. In the case of the low-frequency Lorentzian, it is assumed to be zero-centred ($\nu_{0,2} = 0$), as in the preliminary fitting $\nu_{0,2}$ is consistent with 0. Furthermore, the limiting low frequency of the TPS ($\sim 10^{-5}$ Hz) does not allow for the detection of a defined structure of the broad-band feature to the same precision as in high frequencies and hence an extra free parameter in the form of $\nu_{0,2}$ is considered obsolete. Similarly to Veresvarska et al. (2024b), whereas the low-frequency

⁶ <https://github.com/lightkurve/lightkurve>

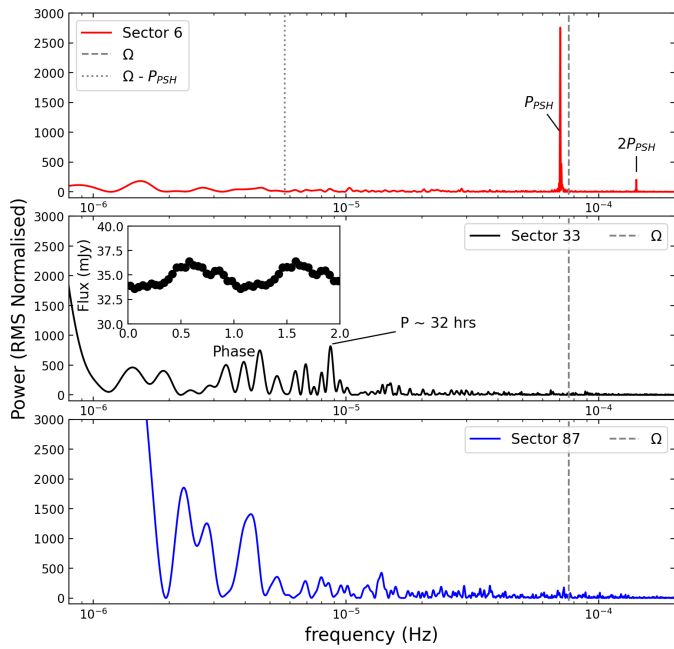


Fig. 12. *TESS* Sector 6 (top), Sector 33 (middle) and Sector 87 (bottom) power spectra. The 3.941-hour period (P_{PSH}) is indicated in the Sector 6 plot together with the first harmonic ($2P_{PSH}$). The Sector 33 plot indicates the low frequency signal at ~ 32 hours, with an inset plot showing the phase-folded light curve on this period. The dashed line indicates the spectroscopic period of 3.645 hours associated with the orbital period.

zero-centred Lorentzian can be fitted, it only represents an upper limit on its intrinsic value.

We perform a fit using the affine-invariant ensemble sampler for Markov chain Monte Carlo (MCMC) as implemented by `emcee` (Foreman-Mackey et al. 2013). We have assumed priors with a small uniform perturbation centred on the best fit values obtained using Levenberg-Marquardt least-squares fitting method. The best fit values with their corresponding errors and reduced χ^2 are detailed in Table 4. The errors correspond to the confidence contours of 99.7% (3σ). The effective peak frequency of the high frequency Lorentzian with corresponding error is also shown in Table 4.

Table 4. Values of the best fit parameters for the TPS in Figure 13 with corresponding errors.

	Sector 33	Sector 87
$A (\times 10^{-2})$	7^{+1}_{-2}	5^{+2}_{-2}
$r_1 (\times 10^{-2})$	$6.3^{+0.2}_{-0.2}$	$6.7^{+0.6}_{-0.7}$
$\Delta_1 (\times 10^{-4})$	$3.8^{+0.5}_{-0.5}$	$4.9^{+0.6}_{-0.5}$
$\nu_{0,1} (\times 10^{-4})$	$6.2^{+0.3}_{-0.3}$	5^{+1}_{-1}
$r_2 (\times 10^{-2})$	$6.6^{+0.4}_{-0.4}$	$13.1^{+0.8}_{-0.8}$
$\Delta_2 (\times 10^{-5})$	$3.4^{+0.9}_{-0.8}$	4^{+1}_{-1}
χ^2_ν	3.2	3.5
$\nu_{max,1} (\times 10^{-4})$	$7.3^{+0.6}_{-0.5}$	7^{+1}_{-1}

3.5. Archival photometry

Archival V -band photometry of SRGt 062340 from the Catalina Real-Time Transients Survey (CRTS, Drake et al. 2009) was obtained between 2005 August 28 and 2013 May 9 and consists of

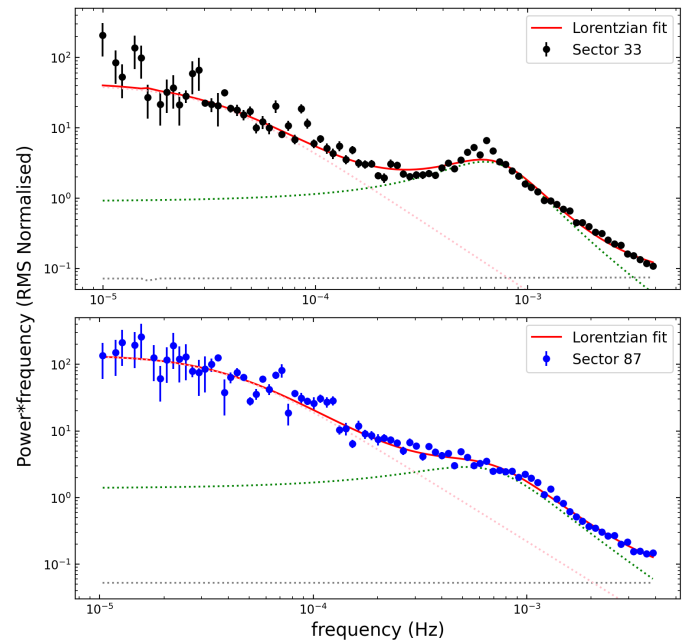


Fig. 13. *TESS* Sector 33 (top) and Sector 87 (bottom) time-averaged power spectra. Both panels include the Lorentzian fit (solid red line) with the individual components shown in dotted lines.

196 observations. Figure 1 show the light curve from the CRTS data in red. There is clear variability, typically $\pm \sim 0.4$ mag for most of the coverage, although there are two dips seen, at HJD 2454065 and HJD 2456362, where the magnitude of the system drops dramatically. Following a gap in the data (HJD 2456042 – HJD 2456294) the object was much fainter than before (by >0.5 mag), reaching a minimum at HJD 2456362 at $V = 13.81$.

Archival ASAS-SN (Kochanek et al. 2017)⁷ differential photometry was found (ASAS-SN Sky Patrol ID: 584115992288), spanning from 2013 October 30 to 2025 May 19, consisting of 6292 observations. The light curve is shown in Figure 1, in blue and green data points, and where the spectroscopic and photometric observations reported on in this study is superimposed. Consult appendix A and text for more detail on the observation epochs, as there is significant overlap for some observations, making it difficult to distinguish between them in the light curve. There is variability, of amplitude $\lesssim 0.5$ mag, for the majority of the ASAS-AN light curve, with a slight dip and then brightening between JD ~ 2458000 – 2459000. However, a significant and sudden decrease in brightness, $\gtrsim 3$ mag, is seen from JD ~ 2460200 . A minimum is reached at JD ~ 2460400 , after which it re-brightens, again with a similarly steep rate as the dimming. There is another dip shortly after; however, it is not as sudden as the first. The system appear to still be in a dip at the last data points. These drops in brightness is reminiscent of the VY Scl class of CV.

4. Discussion

The spectroscopic observations obtained with the SAAO 1.9m telescope in 2021 February and March showed similar broad Balmer absorption lines, whose centres are filled in by prominent narrow emission lines, as was observed with the ANU/WiFeS spectrograph on 2020 October 28 (HJD 2459150.6640), while the He II $\lambda 4686$ and Bowen fluorescence lines were also seen, as

⁷ <https://asas-sn.osu.edu/>

was observed with SALT on October 31 (HJD 2459154.4672) (Schwöpe et al. 2022), albeit at much lower resolution. These Balmer spectral features are similar to what Stickland et al. (1984) observed for the NL CV RZ Gru, even though their study focused more into the far blue and UV, in which they attributed the absorption features to a thick accretion disc, and the narrow emission lines being as a result of the low inclination angle, $i < 20^\circ$, RZ Gru is observed at. The similarities between the spectra of RZ Gru and SRGt 062340 could possibly indicate that it is a UX UMa system seen at a low inclination. UX UMa's are sometimes referred to as 'thick-disc CVs' based on their absorption lines (Warner 1995), and are a subclass of the NL CVs. Skillman et al. (1995) also found similarly low K-amplitude ($25 \pm 4 \text{ km s}^{-1}$) for the emission line radial velocities of MV Lyrae, and concluded that the system is seen at a low inclination ($10^\circ - 13^\circ$). Even though the spectrum that is shown by Skillman et al. (1995) (Figure 1 in their paper) extends further to the red than Figure 2, it is still very similar to what is seen for SRGt 062340. Given this, and the fact that MV Lyrae has a similar orbital period (~ 3.2 hours) as SRGt 062340, further supports our interpretation that SRGt 062340 is likely seen at a very low inclination.

The H β and H γ spectral lines are also similar to those observed in ASAS J071404+7004.3, another bright and nearby NL that has only recently been identified as a CV (Inight et al. 2022), where they also attribute an optically thick accretion disc responsible for the Balmer absorption lines. They propose a disc wind model to explain the strong single-peaked emission lines.

Both optically thick and thin discs, if observed at high inclinations, usually display double peaked emission lines (Horne & Marsh 1986). However, the presence of a disc wind can significantly alter the profile of emission lines, resulting in high-inclination systems to also show single peak emission lines (Honeycutt et al. 1986; Matthews et al. 2015; Tampo et al. 2024). The SALT HRS observations revealed a non-Gaussian profile for the H α emission line, where the strength, primarily of the red peak, is seen to vary slightly on timescales as short as tens of minutes, as revealed in Figure 8. In addition, trailed spectra (Figures B.1 and 7) and photometry show no indication of any kind of eclipse by the secondary star, from which it can be concluded that the inclination of the system must be low enough for the secondary to not eclipse the region where H β or H γ emission is produced, implying $i \lesssim 75^\circ$, and possibly even much smaller given the low amplitude variations in the radial velocity measurements of the emission lines. The decisive feature in the spectrum of ASAS J071704+7004.3 that strongly indicate the presence of a disc wind is the P Cygni profile, seen for He I $\lambda 5876$. There is slight indication of a possible transient P Cygni profile to the He I $\lambda 5876$, line seen from the SALT HRS observations. However, the normalization of the HRS spectra makes it difficult to see any absorption components, even for H β and H γ , where we know from the SpUpNIC observations there is absorption.

The Lomb-Scargle period analysis of ~ 52 hours of high-speed SAAO photometry, taken on 18 nights over a time-base of ~ 4 months, has revealed evidence of a weak (few percent amplitude) period at 24.905 min (Figure 10). While some individual nights show strong period peaks in this region (Figure C.1 in the appendix), they are not always present, which is likely a consequence of the extreme stochastic flickering. Figure C.1 also reveals that numerous flaring and dipping features appear in the light curves which, at first glance, appear identical in shape and duration and therefore might be caused by the same mechanism, but judging from our power spectra these are incoherent varia-

tions, so not orbital or spin phase dependant. This stochastic non-periodic, and often high amplitude, variability is characteristic of flickering in many magnetic CVs, and particularly in some IPs (e.g. TX Col, Buckley & Tuohy 1989). In fact, if the 24.905-min period found from the SAAO photometric measurements is taken to be the spin period, this will give a spin-to-orbital period ratio, $P_{\text{spin}}/P_{\text{orb}}$, of 0.114. Such ratios are typical of IPs (Barrett et al. 1988; Mondal et al. 2022).

Assuming that the orbital period from spectroscopy is 3.645 hours (Section 3.1.2, and in agreement with the period found from X-ray analysis by Cúneo et al. (2026)), the signal in *TESS* Sector 6 could be interpreted as a positive superhump. In the case of positive superhumps, $\frac{1}{P_{\text{PSH}}} < \Omega$, and the signal is associated with the tidal stresses exerted by the secondary star on the accretion disc. These cause the disc to become eccentric and undergo apsidal precession in the prograde direction (Lubow 1991). If this is the case, then we would expect the fundamental precession frequency at $\frac{1}{P_+} = \Omega - \frac{1}{P_{\text{PSH}}} \sim 48$ hours. However, no low frequency signal is detected in *TESS* Sector 6. This may be due to the data quality, as Sector 6 has a low cadence of ~ 30 minutes and the scatter is larger than in Sector 33, where a low frequency periodicity can also be seen by eye in Figure C.2. This unfortunately means that we cannot unambiguously confirm the nature of the signal from Sector 6.

Assuming the signal from Sector 6 is a positive superhump, we can use it to compute the excess $\epsilon = \frac{1/P_{\text{PSH}} - \Omega}{\Omega} \sim 0.081$. Using the relation observed between the superhump excess and orbital period (Patterson 1998) we can show that SRGt 062340 lies on this relation, adding more evidence towards the positive superhump hypothesis. Patterson et al. (2005) extends this relations to higher values of q , with BB Dor $\epsilon = 0.0939(15)$. Equation 8 from Patterson et al. (2005) also allows us to estimate a value of the binary mass ratio q , such that

$$\epsilon = 0.18q + 0.29q^2,$$

from which we obtain $q \sim 0.30$. This would suggest $M_2 \sim 0.24 M_\odot$, assuming that $M_{\text{WD}} \sim 0.8 M_\odot$. This would then place SRGt 062340 in Figure 9 from Patterson et al. (2005) between BB Dor and DW UMa and UU Aqr, in accordance with the observed relation between Ω and ϵ .

If SRGt 062340 is indeed a NL VY Scl system which is compatible with the long-term ASAS-SN light curve, a presence of positive superhumps is unusual. This is because the large disc required for positive superhumps is more easily attained in systems with $P_{\text{orb}} < 2$ hrs due to the compact nature of the systems. However, there are some systems showing photometrically similar behaviour as SRGt 062340. In particular, BB Dor, a NL of similar orbital period to SRGt 062340. In particular, the positive superhump seen in BB Dor is also associated with a similar signal in low frequencies as seen in SRGt 062340 in Sector 33. Another similar NL is DW UMa, which shows only positive superhumps at similar orbital period to SRGt 062340 (Bruch 2023). MV Lyr is another NL at similar orbital period, and also very low orbital inclination (Skillman et al. 1995), resulting in the orbital period not being detectable in *TESS*.

In summary, it is likely that the signal in Sector 6 is a positive superhump, but it cannot be proven with the data at hand. Furthermore, it may be possible that once the system returns to high state the superhump will reappear, allowing a confirmation of this hypothesis.

Flickering, or aperiodic broad-band variability, occurs in all accreting systems (Scaringi et al. 2012b; Uttley & McHardy 2001; Uttley et al. 2005; Van de Sande et al. 2015; Gandhi

2009). Observations confirm this behaviour (Belloni et al. 2002; McHardy et al. 2006; Scaringi et al. 2012a), and it is widely attributed that some flickering could be due to local accretion rate fluctuations propagating inwards on viscous timescales (Lyubarskii 1997; Arévalo & Uttley 2006). Material moves inwards as angular momentum is transferred outwards due to viscous stresses between disc rings, which rotate at different Keplerian velocities (Frank et al. 2002). The standard Shakura-Sunyaev disc model (Shakura & Sunyaev 1973) introduces a dimensionless viscosity parameter, α , often assumed constant. However, flickering likely results from local viscosity fluctuations (Lyubarskii 1997).

The fluctuating accretion disc model has been successfully applied to X-ray binaries, where it describes variability in the optically thin, geometrically thick inner flow (or corona) at X-ray wavelengths (van der Klis 2006), and to CVs at optical wavelengths (Scaringi 2014). In these cases a break feature in the time-averaged power spectrum (TPS) of a light curve displaying flickering shows a ‘break’ which in the framework of propagating viscosity fluctuations can be assumed to occur at viscous timescales, such that the associated frequency is

$$\nu_{visc} = \alpha \left(\frac{H}{R} \right)^2 \sqrt{\frac{GM}{R^3}},$$

where $\frac{H}{R}$ is the scale height ratio at distance R away from the centre of the accretor of mass M and G is the gravitational constant. Assuming that the periods of 24.907 and 28.630 minutes from Section 3.3 are associated with the spin, we can estimate the corresponding dynamical frequency at co-rotation radius R_{CO}

$$R_{CO} = \left(\frac{GMP_{\omega}^2}{4\pi^2} \right)^{1/3},$$

where P_{ω} is the spin period of the system. Assuming that ν_{max} from Table 4 corresponds to the viscous frequency at the co-rotation radius, we can estimate $\alpha \left(\frac{H}{R} \right)^2$ under the assumption of a truncated accretion disc scenario found in IPs and suggested to be present in VY Scl systems by Hameury & Lasota (2002). Given the negligible difference in ν_{max} between Sectors 33 and 87 and the two potential spin periods, we find $\alpha \left(\frac{H}{R} \right)^2 \sim 0.17 - 0.2$. This is slightly lower than the value of ~ 0.7 obtained from modelling the TPS of MV Lyr in Scaringi (2014). This discrepancy aligns with the interpretation of SRGt 062340 as an IP with a truncated accretion disc, in contrast to MV Lyr, which is classified as a standard VY Scl-like system with traces of an inner, hot, geometrically thick, and optically thin flow. Furthermore, our results are consistent with the expectation that $\alpha \left(\frac{H}{R} \right)^2$ decreases with increasing radius (Veresvarska & Scaringi 2023). In order for the break to occur at the WD radius $R_{WD} \sim 0.0099R_{\odot}$, the $\alpha \left(\frac{H}{R} \right)^2 \sim 0.001$, much smaller than the estimated MV Lyr value for inner disc. Whereas this cannot confirm the IP nature of SRGt 062340 or unambiguously determine the spin period, it can serve as circumstantial evidence suggesting that the broad-band structure of the TPS is consistent with an IP-like truncated disc. However, without a firm detection of a spin period, this interpretation remains purely speculative.

The long-term light curves from CRTS and ASAS-SN, Figure 1, reveal long-term low amplitude and slow modulation in brightness, of ~ 0.2 mag as well as dips, ~ 1.5 mag in CRTS and ~ 4 mag in ASAS-SN, which last at least several weeks. VY Scl systems are defined as nova-likes showing a drop in luminosity of mag > 1 (King & Cannizzo 1998), suggesting that SRGt

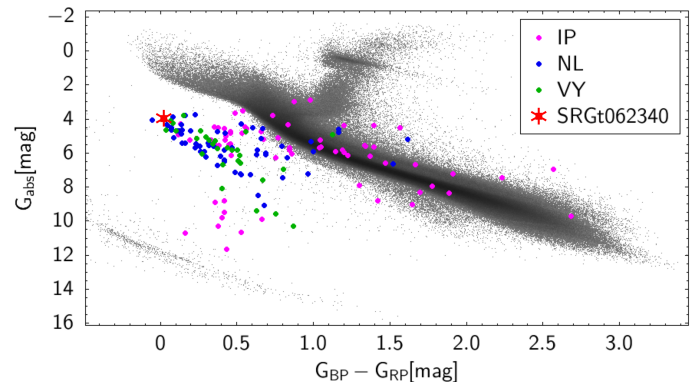


Fig. 14. Gaia colour-magnitude diagram showing the positions of NLs (blue), VY Scl stars (green) and IPs (magenta), with the location of SRGt 062340 indicated by the red star.

062340 belongs to this subgroup. However, these periodic dips in luminosity, together with the low amplitude and slow modulation in the brightness, is consistent with what has also been observed for IPs (Warner 1995; Covington et al. 2022) and therefore an IP interpretation is also plausible. However, because of the lack of a clear and consistent spin period, the IP interpretation cannot be either confirmed or refuted. Polarimetric observations were conducted at the SAAO; however, no significant evidence of polarization was detected (Buckley, private communication). This lack of polarization also cannot definitively rule out the possible IP nature of the system.

Figure 14 show colour-magnitude plots of NL systems, including the VY Scl subclass and IPs, where the colour and distance parameters were obtained from Gaia EDR3. Using the Gaia colour and absolute magnitude clearly indicates that SRGt 062340 is located at the expected region to be a NL system (Dubus & Babusiaux 2024). Based on its position in this colour-magnitude diagram, it appears that SRGt 062340 is more likely to be a VY Scl system than an IP; however, SRGt 062340 seems to be slightly more blue than any VY Scl system in this plot.

Another phenomenon that needs to be considered in interpreting the power spectra of the SAAO photometry is the possible presence of quasi-periodic oscillations, QPOs (Patterson et al. (1977)). Although multiple peaks are seen in the power spectrum of the SAAO photometric observations in the frequency range expected of QPOs (Figure 10), it is not immediately clear whether QPOs are present, since they usually appear as broad and noisy bumps in the power spectra. The changing periodicities found between each individual night’s observations, however, could suggest their presence, although in some IPs, for example TX Col (Buckley & Sullivan (1992), Mhlahlo et al. (2007) and Littlefield et al. (2021)), the purported WD spin period is not always seen to be overwhelmingly prominent, and at times even absent, in period analysis. This is likely due to strong stochastic flickering and the possible presence of red noise. Therefore, the WD spin period might be overwhelmed by the presence of QPO’s on a single night’s observation; however, using all the photometric observations, with a long baseline, the WD spin period is more likely to be detected.

5. Conclusions

For this NL CV, a possible WD spin period of $P_{spin} = 24.905$ min was found from an analysis of high-speed photometric observations, while a $P_{orb} = 3.654$ -hour period was found from time-resolved spectroscopic observations by analysing the $H\beta$ and $H\gamma$

emission line radial velocities. The probable spin-orbital period ratio is $P_{\text{spin}}/P_{\text{orb}} = 0.114$, which places it away from confirmed IPs with orbital periods above the period gap (see Figure 11 in Mukai 2017). The presence of deep dips in brightness seen in long-term light curves (Figure 1), and its location in the colour-magnitude plot (Figure 14), also suggests that SRGt 062340 is more likely a VY Scl system.

The radial velocities of the $H\beta$ and $H\gamma$ emission lines were thoroughly analysed in this study; however, wider wavelength coverage of time-resolved spectroscopic observations that include longer wavelength such as the $H\alpha$ line could help to confirm the orbital period of the system. SALT HRS observations were obtained, which included $H\alpha$; however, these observations were taken to study the morphology of the emission lines, and showed that, at least for $H\alpha$, the lines show slight indication of having a non-Gaussian morphology, and of having a high-velocity component in some spectra. These observations also revealed that the morphology of the $H\alpha$ emission line does seem to change; however, longer coverage per night is needed to determine whether these changes are phase related. No sign of emission from the irradiated face of the secondary star was however seen. In addition, UV observations (e.g. with HST) could reveal disc wind features (such as P-Cygni profiles) often more easily seen at shorter wavelengths.

Acknowledgements. JB acknowledges support from the *Deutsche Forschungsgemeinschaft*, DFG project number Ts 17/2-1, and the South African National Research Foundation (NRF). Some of the observations reported in this paper were obtained with the Southern African Large Telescope (SALT) under program 2021-2-LSP-001 (PI: D. Buckley). Polish participation in SALT is funded by grant No. MEiN nr 2021/WK/01. We thank the South African Astronomical Observatory for generous allocations of observing time. MV acknowledges the support of the Science and Technology Facilities Council (STFC) studentship ST/W507428/1. VAC acknowledges support from the Deutsches Zentrum für Luft- und Raumfahrt (DLR) under contract number 50 OR 2405

References

Arévalo, P. & Uttley, P. 2006, MNRAS, 367, 801

Astropy Collaboration, Price-Whelan, A. M., Lim, P. L., et al. 2022, ApJ, 935, 167

Bailer-Jones, C. A. L., Rybizki, J., Fouesneau, M., Demleitner, M., & Andrae, R. 2021, AJ, 161, 147

Banse, K., Crane, P., Grosbol, P., et al. 1983, The Messenger, 31, 26

Barnes, S., Cottrell, P., Albrow, M., et al. 2008, in Ground-based and Airborne Instrumentation for Astronomy II, Vol. 7014, SPIE, 247–258

Barrett, P., O'Donoghue, D. D., & Warner, B. 1988, MNRAS, 233, 759

Belloni, T., Psaltis, D., & van der Klis, M. 2002, ApJ, 572, 392

Bowman, D. M. & Holdsworth, D. L. 2019, A&A, 629, A21

Bruch, A. 2023, MNRAS, 519, 352

Buckley, D. & Sullivan, D. 1992, in Cataclysmic Variable Stars, Vol. 29, 387

Buckley, D. A., Swart, G. P., & Meiring, J. G. 2006, in Ground-based and Airborne Telescopes, Vol. 6267, SPIE, 333–347

Buckley, D. A. H. & Tuohy, I. R. 1989, ApJ, 344, 376

Covington, A. E., Shaw, A. W., Mukai, K., et al. 2022, ApJ, 928, 164

Crause, L. A., Carter, D., Daniels, A., et al. 2016, in Ground-based and Airborne Instrumentation for Astronomy VI, Vol. 9908, SPIE, 698–716

Crause, L. A., Sharples, R. M., Bramall, D. G., et al. 2014, in Ground-based and Airborne Instrumentation for Astronomy V, Vol. 9147, SPIE, 2138–2151

Crawford, S. M., Still, M., Schellart, P., et al. 2010, in Observatory Operations: Strategies, Processes, and Systems III, Vol. 7737, SPIE, 550–561

Cúneo, V. A., Muñoz-Darias, T., Jiménez-Ibarra, F., et al. 2023, A&A, 679, A85

Cúneo, V. A., Schwöpe, A. D., Kurpas, J., et al. 2026, A&A, 705, A71

Dopita, M., Rhee, J., Farage, C., et al. 2010, Ap&SS, 327, 245

Drake, A., Djorgovski, S., Mahabal, A., et al. 2009, ApJ, 696, 870

Dubus, G. & Babusiaux, C. 2024, A&A, 683, A247

Foreman-Mackey, D., Hogg, D. W., Lang, D., & Goodman, J. 2013, PASP, 125, 306

Frank, J., King, A., & Raine, D. 2002, Accretion Power in Astrophysics, 3rd edition (Cambridge University Press)

Gandhi, P. 2009, ApJ, 697, L167

Hameury, J. M. & Lasota, J. P. 2002, A&A, 394, 231

Harlaftis, E. T. & Horne, K. 1999, MNRAS, 305, 437

Hellier, C. 2001, Cataclysmic Variable Stars-how and why they vary (Springer Science & Business Media)

Honeycutt, R. K., Schlegel, E. M., & Kaitchuck, R. H. 1986, ApJ, 302, 388

Horne, K. & Marsh, T. 1986, MNRAS, 218, 761

Ingle, K., Gänsicke, B., Blondel, D., et al. 2022, MNRAS, 510, 3605

King, A. R. & Cannizzo, J. K. 1998, ApJ, 499, 348

Knizář, A., Gvaramadze, V., & Berdníkov, L. 2016, MNRAS, 459, 3068

Kochanek, C. S., Shappee, B. J., Stanek, K. Z., et al. 2017, PASP, 129, 104502

Lightkurve Collaboration, Cardoso, J. V. d. M., Hedges, C., et al. 2018, Lightkurve: Kepler and TESS time series analysis in Python, *Astrophysics Source Code Library*

Littlefield, C., Scaringi, S., Garnavich, P., et al. 2021, AJ, 162, 49

Lomb, N. R. 1976, Ap&SS, 39, 447

Lubow, S. H. 1991, ApJ, 381, 259

Lyubarskii, Y. E. 1997, MNRAS, 292, 679

Matthews, J. H., Knigge, C., Long, K. S., Sim, S. A., & Higginbottom, N. 2015, MNRAS, 450, 3331

McHardy, I. M., Koerding, E., Knigge, C., Uttley, P., & Fender, R. P. 2006, Nature, 444, 730

Mhlahlo, N., Buckley, D., Dhillon, V., et al. 2007, MNRAS, 380, 133

Mondal, S., Ponti, G., Haberl, F., et al. 2022, A&A, 666, A150

Mukai, K. 2017, PASP, 129, 062001

Newville, M., Stensitzki, T., Allen, D. B., et al. 2016

Patterson, J. 1998, PASP, 110, 1132

Patterson, J., Kemp, J., Harvey, D. A., et al. 2005, PASP, 117, 1204

Patterson, J., Robinson, E. L., & Nather, R. E. 1977, ApJ, 214, 144

Pavlinsky, M., Tkachenko, A., Levin, V., et al. 2021, A&A, 650, A42

Predehl, P., Andritschke, R., Arefiev, V., et al. 2021, A&A, 647, A1

Ricker, G. R., Winn, J. N., Vanderspek, R., et al. 2014, *Journal of Astronomical Telescopes, Instruments, and Systems*, 1, 014003

Scargle, J. D. 1982, ApJ, 263, 835

Scaringi, S. 2014, MNRAS, 438, 1233

Scaringi, S., Körding, E., Uttley, P., et al. 2012a, MNRAS, 427, 3396

Scaringi, S., Körding, E., Uttley, P., et al. 2012b, MNRAS, 421, 2854

Schachter, J., Filippenko, A. V., Kahn, S. M., & Paerels, F. 1991, ApJ, 373, 633

Schwöpe, A., Buckley, D. A., Kawka, A., et al. 2022, A&A, 661, A42

Schwöpe, A. D. 2025, A&A, 698, A106

Shakura, N. I. & Sunyaev, R. A. 1973, A&A, 55, 155

Shappee, B. J., Prieto, J. L., Grupe, D., et al. 2014, ApJ, 788, 48

Skillman, D. R., Patterson, J., & Thorstensen, J. R. 1995, PASP, 107, 545

Stickland, D., Kelly, B., Cooke, J., et al. 1984, MNRAS, 206, 819

Sunyaev, R., Arefiev, V., Babyshkin, V., et al. 2021, A&A, 656, A132

Tampo, Y., Knigge, C., Long, K. S., Matthews, J. H., & Segura, N. C. 2024, MNRAS, 532, 1199

Tody, D. 1986, in *Instrumentation in astronomy VI*, Vol. 627, SPIE, 733–748

Uttley, P. & McHardy, I. M. 2001, MNRAS, 323, 1

Uttley, P., McHardy, I. M., & Vaughan, S. 2005, MNRAS, 359, 345

Van de Sande, M., Scaringi, S., & Knigge, C. 2015, MNRAS, 448, 2430

van der Klis, M. 2006, *Rapid X-ray variability* (NATO Advanced Study Institutes Series. Series C, Mathematical and Physical Sciences), 39–112

VanderPlas, J. T. & Ivezić, Ž. 2015, *The Astrophysical Journal*, 812, 18

Veresvarska, M. & Scaringi, S. 2023, MNRAS, 518, 5576

Veresvarska, M., Scaringi, S., Hagen, S., et al. 2024a, MNRAS, 529, 664

Veresvarska, M., Scaringi, S., Knigge, C., et al. 2024b, MNRAS, 534, 3087

Warner, B. 1995, *Cataclysmic variable stars*, Vol. 28 (Cambridge University Press)

Zurek, D. R., Knigge, C., Maccarone, T. J., Dieball, A., & Long, K. S. 2009, ApJ, 699, 1113

Appendix A: Observing logs

Table A.1. SAAO 1.9m SpUpNIC spectroscopic observations

Date	HJD (start)	N (observations)	Exposure Time (seconds)	Duration (minutes)	Grating Angle	Wavelength Coverage (Å)
2021-02-02	2459248.2966	9	1200	192.65	5.50	3795 - 5025
2021-02-26	2459272.2721	54	300	299.97	4.20	4116 - 5326
2021-02-27	2459273.2577	60	300	322.57	4.20	4116 - 5326
2021-03-02	2459276.2542	54	300	289.63	4.20	4116 - 5326
2021-03-17	2459291.2892	15	300	156.55	5.50	3762 - 4990
2021-03-18	2459292.2858	24	300	155.05	5.50	3760 - 4992
2021-03-19	2459293.2916	20	300	128.50	5.50	3768 - 5000
2021-03-20	2459294.2814	10	300	62.68	5.50	3768 - 5000
2021-03-21	2459295.3110	20	300	123.10	5.50	3800 - 5029
2021-03-22	2459296.2745	28	300	170.85	5.50	3800 - 5029

Table A.2. SAAO photometric observation log

Date	BJD (start)	Exposure Time (seconds)	Duration (hours)	Filter	Telescope	SHOC Camera
2020-11-01	2459155.5004	0.3	3.213	clear	40 inch	SHA
2020-11-02*	2459156.5195	1.0	2.407	clear	40 inch	SHA
2020-11-03*	2459157.5407	0.3	1.046	clear	40 inch	SHA
2020-11-27	2459181.4112	2.0	3.102	clear	Lesedi	SHD
2020-11-28	2459182.3333	2.0	1.905	clear	Lesedi	SHD
2020-11-29	2459183.3305	2.0	6.084	clear	Lesedi	SHD
2020-12-03*	2459187.5572	5.0	0.202	g'	40 inch	SHA
2020-12-04*	2459188.4346	10.0	0.707	clear	40 inch	SHA
2021-01-04	2459219.5329	1.0	1.580	clear	40 inch	SHA
2021-01-13	2459228.3549	1.0	5.682	clear	40 inch	SHA
2021-01-20	2459235.3732	1.0	5.065	clear	40 inch	SHA
2021-02-01	2459247.4396	1.0	1.244	clear	Lesedi	SHD
2021-02-02	2459248.2718	1.0	1.419	clear	Lesedi	SHD
2021-02-26	2459272.2984	1.0	4.146	clear	Lesedi	SHD
2021-02-27	2459273.3171	1.0	4.216	g'	40 inch	SHA
2021-02-27	2459273.2633	1.0	4.919	clear	Lesedi	SHD
2021-03-02	2459276.3000	5.0	4.485	g'	40 inch	SHA
2021-03-02	2459276.2462	1.0	5.092	r'	Lesedi	SHD

* Observation of poor quality and was not used in analysis

Table A.3. SALT HRS observations

Date	JD (start)	N (observations)	Exposure Time (seconds)	Duration (minutes)	Wavelength Coverage (Å)
2023-11-09	2460258.4463	4	600	43.5	3734 - 8789
2023-11-28	2460277.3959	2	600	21.2	3764 - 8789
2023-11-29	2460278.3915	2	600	21.2	3764 - 8789
2023-11-30	2460279.3943	2	600	21.2	3764 - 8789
2023-12-07	2460286.3732	2	600	21.2	3764 - 8789
2023-12-14	2460293.3488	4	600	43.5	3764 - 8789
2024-01-13	2460323.4995	4	600	43.5	3764 - 8789
2024-01-15	2460325.4968	4	600	43.5	3764 - 8789
2024-01-20	2460330.4830	4	600	21.2	3764 - 8789
2024-01-31	2460341.4521	4	600	43.5	3764 - 8789
2024-03-19	2460389.3187	4	600	43.5	3764 - 8789
2024-03-29	2460399.2967	4	600	43.5	3764 - 8789
2024-04-02	2460403.2837	4	600	43.5	3764 - 8789
2024-04-04	2460405.2806	4	600	43.5	3764 - 8789

Appendix B: Spectroscopy

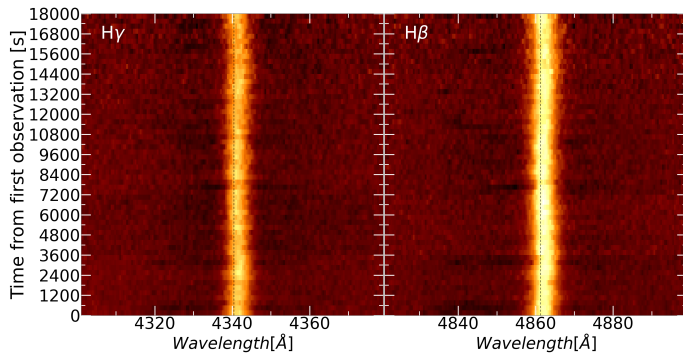


Fig. B.1. Trailed spectra of $H\gamma$ (left) and $H\beta$ (right) from 2021 February 27. The vertical dashed black lines coincide with the respective rest wavelengths, which show that the peak of the emission lines lie slightly towards longer wavelengths. Note the wider darker regions of the absorption lines, adjacent to both sides of the bright emission lines, and the sporadic stronger absorption.

Table B.1. Averaged emission line width measurements

	$H\beta$	$He\text{ II } \lambda 4686$	$H\gamma$
Date	FWHM (km s $^{-1}$)		
2021 February 2	337 ± 8	394 ± 28	366 ± 9
2021 February 26	318 ± 8	403 ± 26	321 ± 8
2021 February 27	313 ± 9	414 ± 26	324 ± 8
2021 March 2	327 ± 8	403 ± 25	327 ± 7
2021 March 17	317 ± 7	403 ± 24	307 ± 9
2021 March 18	313 ± 11	394 ± 40	306 ± 11
2021 March 19	317 ± 9	399 ± 23	308 ± 10
2021 March 20	303 ± 7	394 ± 23	291 ± 8
2021 March 21	310 ± 8	402 ± 25	315 ± 7
2021 March 22	310 ± 9	404 ± 26	309 ± 9

Table B.2. Averaged absorption line width measurements

	$H\beta$	$H\gamma$
Date	FWHM (km s $^{-1}$)	
2021 February 2	4356 ± 309	3295 ± 140
2021 February 26	4213 ± 234	2831 ± 207
2021 February 27	4133 ± 256	2747 ± 213
2021 March 2	4230 ± 215	2989 ± 184
2021 March 17	4099 ± 174	2791 ± 147
2021 March 18	4180 ± 331	3112 ± 345
2021 March 19	4089 ± 248	2773 ± 212
2021 March 20	3927 ± 219	2692 ± 170
2021 March 21	4218 ± 270	3389 ± 298
2021 March 22	4405 ± 359	3243 ± 322

Table B.3. SALT HRS radial velocity measurements

HJD (mid)	ϕ	$H\alpha$ Blue (km s $^{-1}$)	$H\alpha$ Red (km s $^{-1}$)
2460258.452078	0.102	-17.4 ± 0.8	98.5 ± 3.2
2460258.459823	0.161	-4.5 ± 0.8	110.9 ± 3.1
2460258.467589	0.220	1.9 ± 1.5	94.2 ± 3.7
2460258.475343	0.278	5.4 ± 3.3	81.6 ± 6.7
2460277.402424	0.807	10.8 ± 1.2	167.4 ± 7.3
2460277.410190	0.866	-6.0 ± 1.2	124.3 ± 3.2
2460278.398117	0.357	15.8 ± 2.1	87.3 ± 1.8
2460278.405872	0.416	-15.8 ± 3.0	83.9 ± 2.7
2460279.400951	0.962	16.3 ± 1.4	115.0 ± 3.5
2460279.408705	0.021	23.5 ± 0.6	170.8 ± 2.2
2460286.379980	0.886	-21.0 ± 1.0	137.1 ± 4.3
2460286.387734	0.944	-24.9 ± 0.9	136.4 ± 3.2
2460293.355776	0.785	-18.9 ± 0.9	119.0 ± 4.3
2460293.363530	0.843	-10.0 ± 0.9	151.8 ± 4.0
2460293.371297	0.902	-13.8 ± 1.2	140.5 ± 4.1
2460293.379051	0.961	-16.2 ± 1.1	122.2 ± 2.8
2460323.506512	0.425	-40.4 ± 2.9	94.5 ± 1.8
2460323.514279	0.483	-41.8 ± 2.1	87.2 ± 1.7
2460323.522045	0.542	-35.1 ± 1.2	91.2 ± 1.7
2460323.529810	0.601	-36.1 ± 1.5	84.9 ± 2.7
2460325.503746	0.570	-6.7 ± 2.3	94.0 ± 2.0
2460325.511501	0.629	-2.6 ± 3.4	88.4 ± 3.4
2460325.519267	0.688	-21.3 ± 5.0	68.0 ± 4.7
2460325.527010	0.746	0.4 ± 4.2	96.0 ± 11.4
2460330.489833	0.381	24.2 ± 3.3	121.3 ± 2.1
2460330.497588	0.439	-17.0 ± 3.5	98.7 ± 1.4
2460330.505342	0.498	-60.9 ± 4.0	71.9 ± 1.4
2460330.513096	0.557	30.9 ± 2.7	97.3 ± 2.3
2460341.458632	0.559	-22.8 ± 2.3	88.9 ± 3.3
2460341.466399	0.618	-27.1 ± 4.0	92.4 ± 4.5
2460341.474175	0.677	-39.2 ± 2.9	94.5 ± 3.3
2460341.481942	0.736	-18.5 ± 2.8	119.6 ± 4.2
2460389.322768	0.524	-5.5 ± 3.0	108.0 ± 4.2
2460389.330521	0.583	9.9 ± 2.4	126.9 ± 4.7
2460389.338288	0.642	-1.1 ± 2.7	123.9 ± 4.5
2460389.346041	0.701	6.6 ± 3.0	142.1 ± 5.0
2460399.300144	0.185	-32.5 ± 7.2	100.4 ± 4.3
2460399.307899	0.244	-57.8 ± 9.0	87.3 ± 4.3
2460399.315676	0.303	-29.2 ± 15.2	97.5 ± 6.8
2460399.323442	0.361	-23.0 ± 22.1	93.9 ± 6.4
2460403.286812	0.417	-64.8 ± 16.5	91.0 ± 5.1
2460403.294578	0.475	-86.8 ± 20.0	80.2 ± 5.9
2460403.302355	0.534	-13.1 ± 24.2	96.3 ± 18.3
2460403.310109	0.593	14.1 ± 24.2	114.7 ± 26.8
2460405.283607	0.559	7.0 ± 13.9	96.7 ± 15.6
2460405.291373	0.618	11.8 ± 5.5	123.4 ± 12.5
2460405.299138	0.676	-3.0 ± 3.3	128.5 ± 6.6
2460405.306904	0.735	9.1 ± 2.1	178.6 ± 6.2

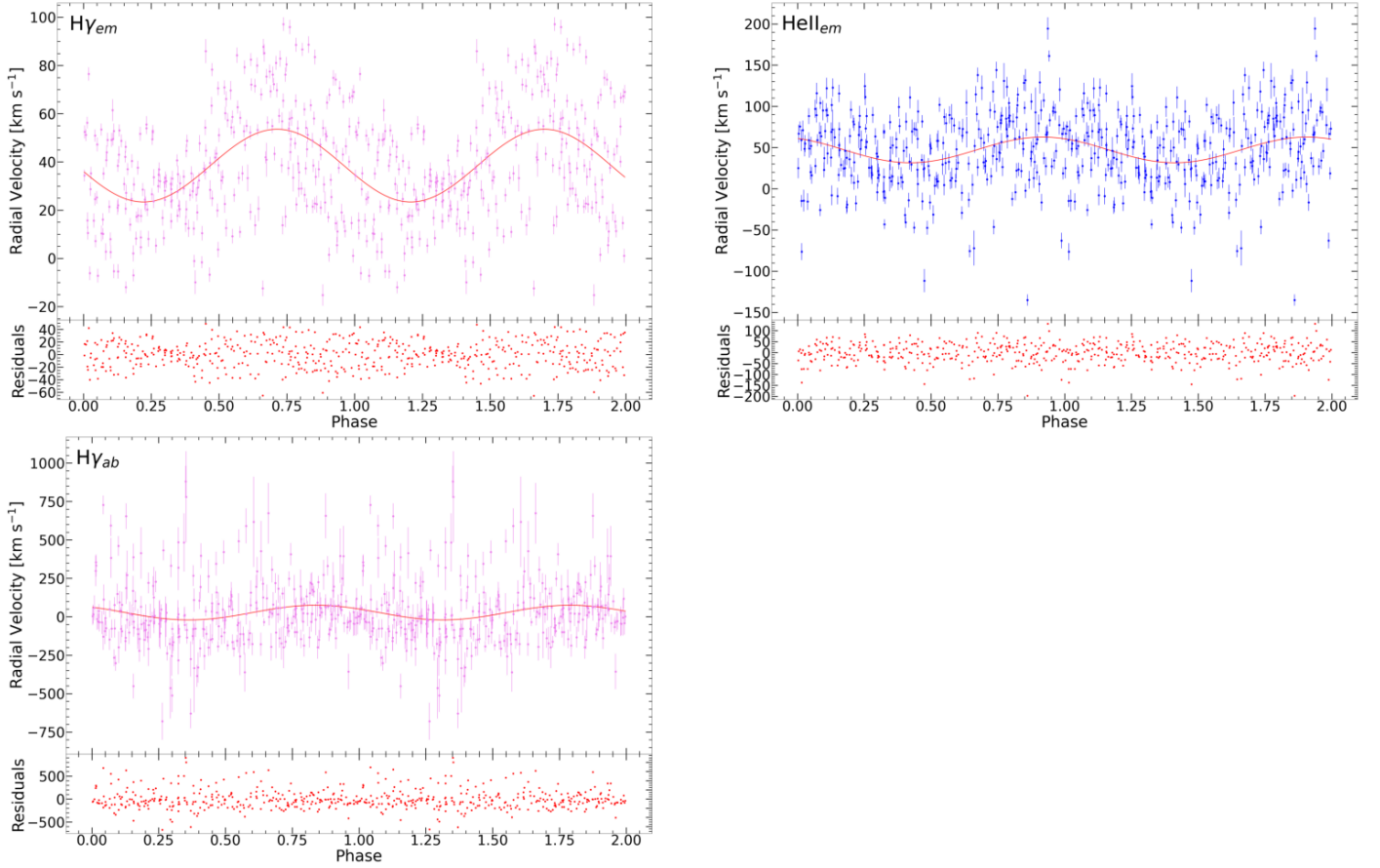


Fig. B.2. H γ emission (H γ_{em} , top left) and absorption (H γ_{ab} , bottom left) line radial velocities phase-folded on the 3.645-hour period, with the phase-folded He II $\lambda 4686$ emission line radial velocities at top right. The fitted sine functions, with the parameters in Table 2, are also shown, with the residuals in the lower panels of each plot.

Table B.4. SALT HRS phase-folded binned radial velocity measurements

ϕ (mid bin)	H α Blue (km s $^{-1}$)	H α Red (km s $^{-1}$)
0.05	23.4 ± 0.6	170.8 ± 2.2
0.15	-11.9 ± 0.7	103.6 ± 2.4
0.25	2.4 ± 1.9	89.7 ± 4.0
0.35	19.3 ± 3.1	105.9 ± 2.3
0.45	-39.8 ± 2.1	84.3 ± 1.2
0.55	-20.0 ± 2.5	87.0 ± 2.5
0.65	-21.8 ± 2.2	87.0 ± 2.7
0.75	-7.0 ± 1.3	126.5 ± 3.6
0.85	-12.9 ± 0.8	120.4 ± 3.2
0.95	-9.0 ± 0.8	116.7 ± 2.2

Appendix C: Photometry

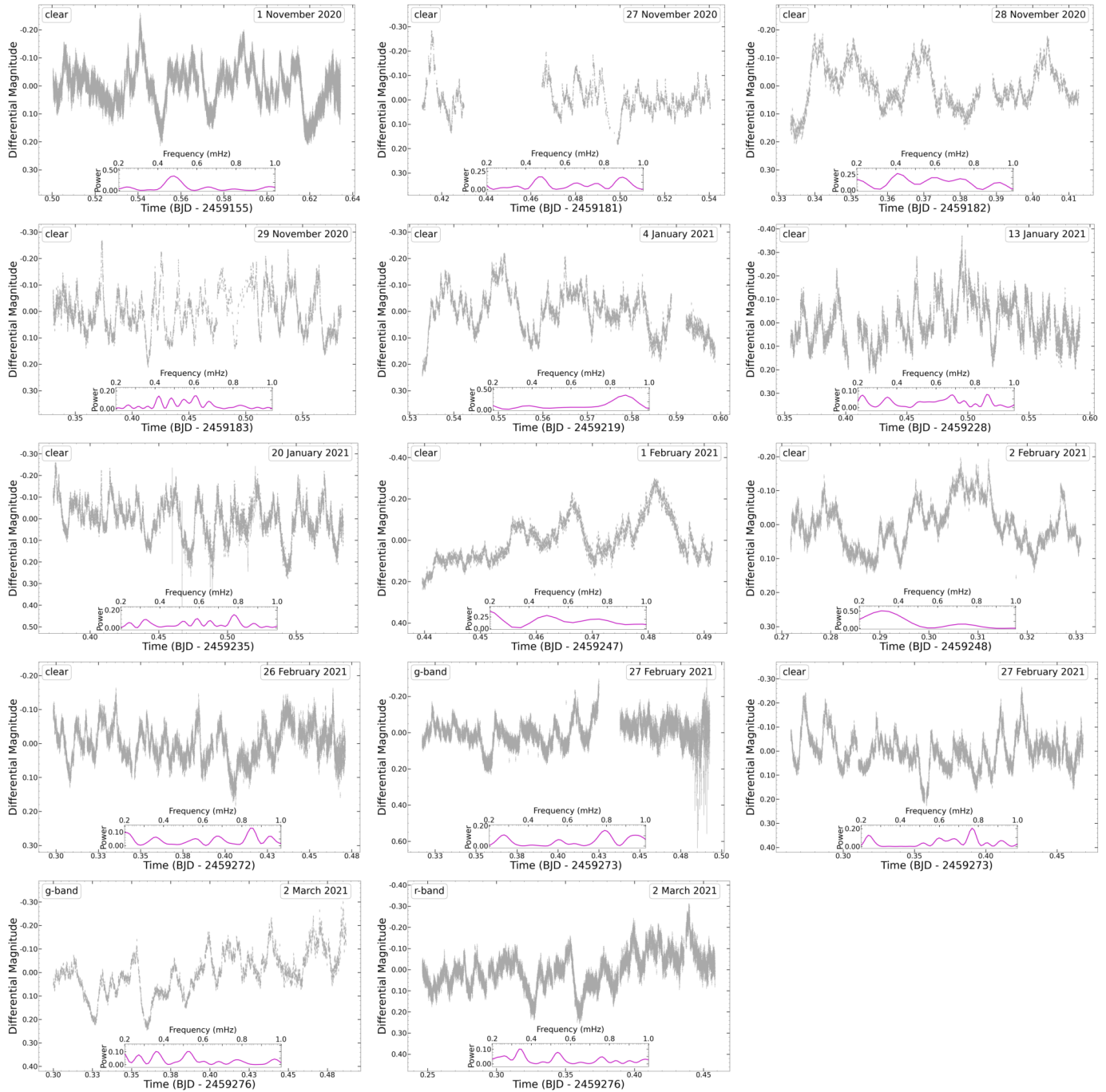
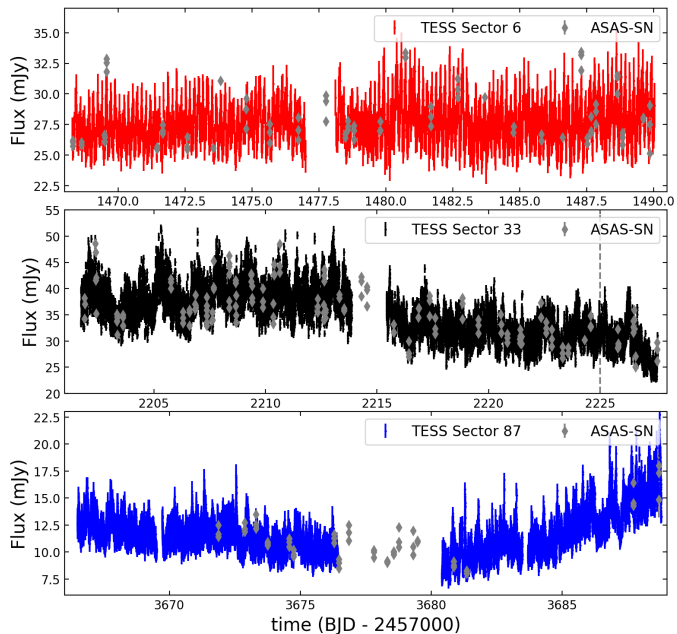
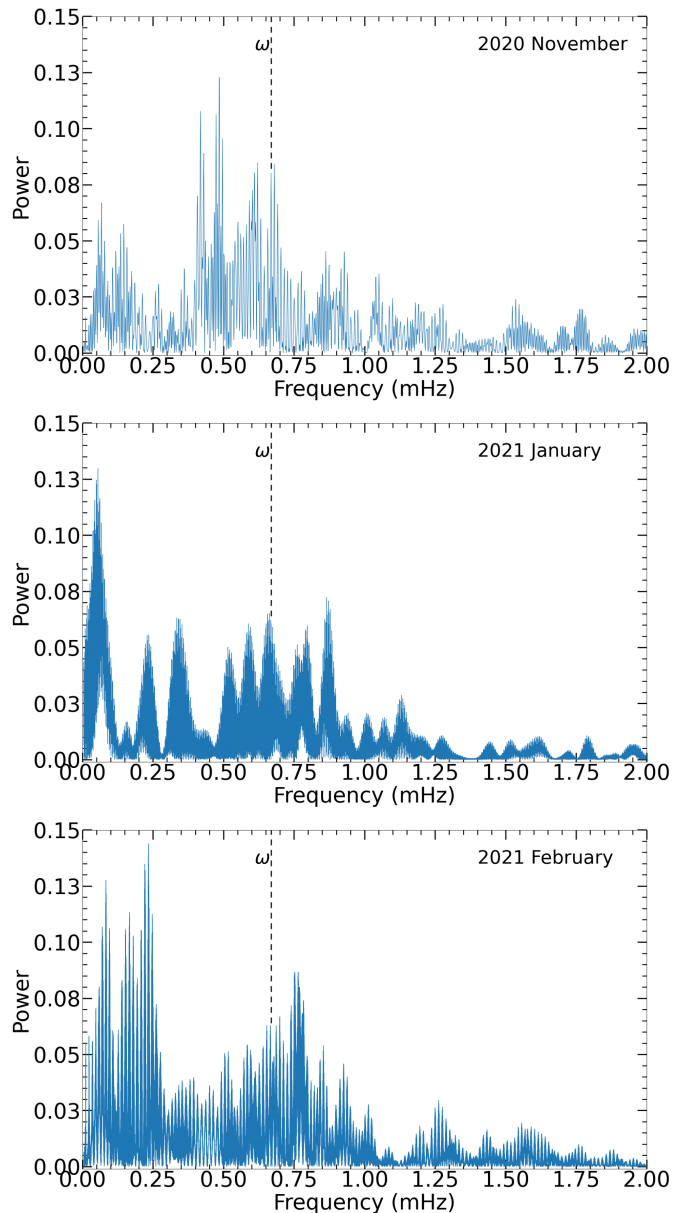


Fig. C.1. Light curve plots from all photometric observations. The filter used for the observations is found in the top left corner of each respective figure. The inset plot shows the power spectrum from Lomb-Scragle period analysis.

Table C.1. Differential photometry periods

Date	Filter	Orbits Covered	Period (hours)
2020 November 1	clear	1.015	0.580 ± 0.006
2020 November 27	clear	0.980	0.586 ± 0.022
2020 November 28	clear	0.602	0.670 ± 0.055
2020 November 29	clear	1.922	0.457 ± 0.101
2021 January 4	clear	0.499	0.317 ± 0.035
2021 January 13	clear	1.795	4.524 ± 0.212
2021 January 20	clear	1.600	0.356 ± 0.030
2021 February 1	clear	0.393	1.556 ± 0.039
2021 February 2	clear	0.448	0.858 ± 0.028
2021 February 26	clear	1.310	2.896 ± 0.036
2021 February 27	g'	1.332	3.378 ± 0.026
2021 February 27	clear	1.554	0.361 ± 0.086
2021 March 2	g'	1.417	5.606 ± 0.069
2021 March 2	r'	1.609	6.365 ± 0.328

**Fig. C.2.** TESS Sector 6 (top), Sector 33 (middle), and Sector 87 (bottom) light curves. The grey diamonds represent ASAS-SN g -band observations. The vertical dashed grey line in the middle panel shows a cut-off point, after which the light curve was no longer stationary, and hence excluded from analysis.**Fig. C.3.** Lomb-Scargle power spectra of the clear filter photometric observations. The observations were divided into three groups, the combined observations obtained in 2020 November (top panel), those obtained in 2021 January (middle panel) and those obtained in 2021 February (bottom panel). In each panel, the spin frequency of the WD is indicated by the dashed line labelled ω , and show that some power is seen in each grouping at ω . It is evident from these three groupings that there is significant change in the power spectrum on short (weeks, or shorter) timescales, which could be interpreted as showing evidence of QPOs.

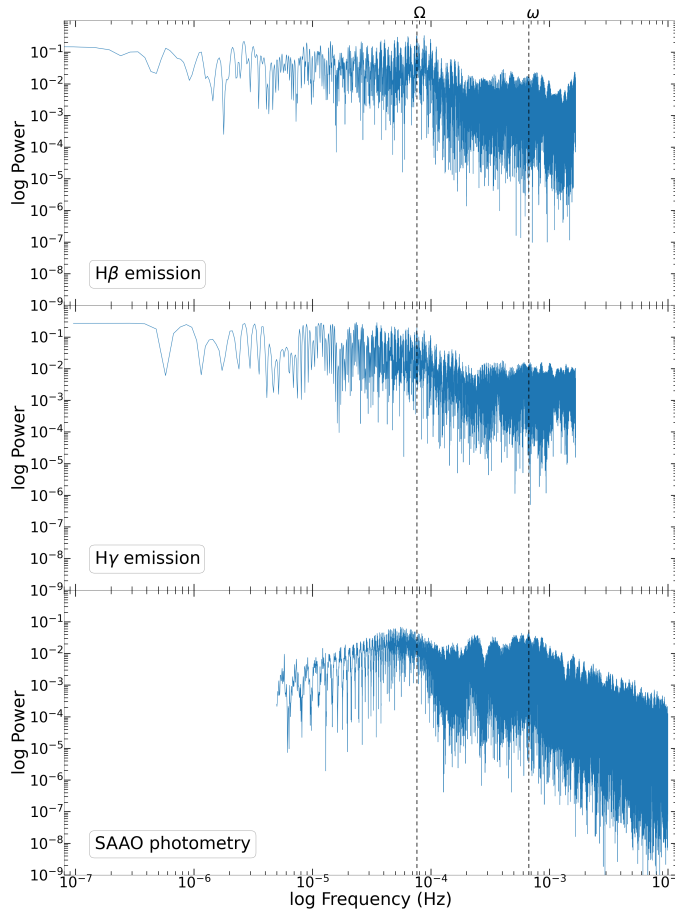


Fig. C.4. Log-log power spectra of the $H\beta$ emission line radial velocities (top), Hy emission (middle), and the SAAO photometric observations (bottom). Each panel extends to the respective Nyquist frequency of the observation. The dashed vertical lines indicate the spectroscopic orbital, Ω , and spin, ω , frequencies, respectively.